scientific reports

Check for updates

OPEN

Anticorrosive performance of newly synthesized dipyridine based ionic liquids by experimental and theoretical approaches

Amira Hossam Eldin Moustafa[1]✉, Hanaa H. Abdel-Rahman[1], Mohamed Hagar[1,2], Mohamed R. Aouad[3], Nadjet Rezki[3] & Sherif A. A. Bishr[1]

Two newly synthetic nontoxic dipyridine-based ionic liquids (P_{ILs}) with the same chain lengths and different polar groups were investigated: bispyridine-1-ium tetrafluoroborate (BPHP, TFPHP) with terminal polar groups *Br* and CF_3, respectively, on Carbon steel (CS) in 8M H_3PO_4 as corrosion inhibitors. Their chemical structure was verified by performing ^{1}HNMR and ^{13}CNMR. Their corrosion inhibition was investigated by electrochemical tests, especially as mass transfer with several characterizations: Scanning electron microscope/Energy dispersive X-ray spectroscopy (SEM–EDX), UV–visible, Atomic force microscope, Atomic absorbance spectroscopy, X-ray Photoelectron Spectroscopy and Gloss value. Theoretical calculation using density functional theory by calculating several parameters, molecular electrostatic potential, Fukui Indices, and Local Dual Descriptors were performed to demonstrate the reactivity behavior and the reactive sites of two molecules with a concentration range ($1.25–37.5 \times 10^{-5}$ M) and temperature (293–318 K). The maximum inhibition efficiency (76.19%) and uniform coverage were sufficient for BPHP at an optimum concentration of 37.5×10^{-5} M with the lowest temperature of 293 K. TFPHP recorded 71.43% at the same conditions. Two P_{ILs} were adsorbed following the El-Awady adsorption isotherm, including physicochemical adsorption. The computational findings agree with Electrochemical measurements and thus confirm CS's corrosion protection in an aggressive environment.

The damage by corrosion generates high inspection, repair, and replacement costs, constituting a public risk. Many techniques were explored to control this issue. Applying corrosion inhibitors has proven to be the most efficient method for increasing these materials' corrosion resistance and minimizing the harm they cause[1]. The corroding surfaces immediately become rough after the corrosion assault begins, significantly affecting the diffusion-controlled corrosion rate. Furthermore, when the generated corrosion layer is highly porous, surface roughness greatly increases the mass transfer rate of O_2 to the electrodes of the electrochemical corrosion cell, resulting in higher corrosion rates. The most popular approach for controlling corrosion is the creation of novel chemicals that act as corrosion inhibitors, especially in acid media, due to several technical and financial benefits. The efficiency of these chemical compounds is affected by various factors, including temperature, humidity, shear stresses caused by fluid flow, and others. This kind of corrosion inhibitor is an organic chemical substance shielding the metallic substrate by generating an adsorbed layer that prevents water molecules and other corrosive species from reaching the surface[2]. The inhibition effectiveness depends on the ability of the inhibitor/surface system to form an adhesive and continuous layer and isolate the surface from the corrosive environment, thus decreasing the corrosion rate. The polar functional groups and the intermolecular interactions between the inhibitor molecules play a crucial role[3–5]. Based on the interaction strength between surface and inhibitor, the inhibitor compounds have been described by two kinds of interactions that corrosion inhibitors can use to adsorb at the interface: as being chemisorbed, which occurs when inhibitors and d-orbitals of the iron surface share electrons, and physisorbed, which occurs when charged molecules interact electrostatically with the metal surface.

[1]Chemistry Department, Faculty of Science, Alexandria University, P.O. 426 Ibrahemia, Alexandria 21321, Egypt. [2]Faculty of Advanced Basic Sciences, Alamein International University, Alamein, Matrouh Governorate, Egypt. [3]Chemistry Department, College of Science, Taibah University, 30002 Al-Madinah Al-Munawarah, Saudi Arabia. ✉email: Amira.mostafa@alexu.edu.eg; amirahossameldin79@yahoo.com

Carbon steel (CS) is frequently used in various industries as the preferred construction material because it is less expensive than corrosion-resistant alloys. CS must be protected from corrosion because it has a broad scope of applications in industries, including power plants, the petroleum industry, and building materials, as it is cost-effective and imparts high mechanical strength[3,6–8]. CS is frequently used as a structural component in industrial pipes, buildings, bridges, and kitchen appliances. CS is unstable chemically and reacts chemically or electrochemically with its surrounding environments to produce more stable corrosion products. In contrast, metal corrosion has always been a hot topic for researchers because of the risks to safety and the financial losses it causes to the industry, the way corrosion costs governments a lot of money[9].

Acid solutions are generally used to remove undesirable scale and rust in several industrial processes. Because it is less corrosive than other mineral acids, Phosphoric acid (H_3PO_4) is a significant industrial chemical used as an intermediate in the fertilizer industry for metal surface treatment in the metallurgical industry. It is used for processes like chemical and electrolytic polishing or etching, chemical colouring, removing oxide film, phosphating, passivating, and surface cleaning. Despite its importance, it shows strong corrosiveness on CS. So, adding anti-corrosion materials slowed or inhibited the CS corrosion in phosphoric acid. Inhibitors are used in these processes to control metal dissolution as well as acid consumption[10–13].

Therefore, adding an excellent inhibitor to an acidic environment is one of the best options. Many researchers are interested in the chemistry of ionic liquids (P_{ILs}), which have collected extraordinary interest as powerful and have cautiously started on the more difficult challenge of industrial-oriented synthesis because they consider them corrosion inhibitors of green chemistry, thermal stable, have a strong adsorbent defence on the metal surface[14–19]. P_{ILs} have several advantageous physiochemical properties, including non-toxic, high conductivity, non-flammability, high thermal and chemical stability[19–25], and environmentally friendly and non-hazardous due to their non-negligible vapor pressure. Additionally, P_{ILs} are highly soluble in polar corrosive environments due to their ionic nature. It is understandable that P_{ILs} with various cationic and/or anionic counters and show different side chains and cationic headgroups have been the interest of researchers in medicinal chemistry[26–32], catalysis[33], preventing certain metals and alloys from corroding[34], electrochemistry[35], biological activity in drug delivery and synthesis of drugs[36], fuel production and processing[37,38], liquid crystal development[39], biotechnology[40], and other chemical processes. P_{ILs} are salts combining organic cations like pyridazinium, imidazolium, and pyrrolidinium with inorganic anions like chloride, bromide, and iodide. Pyridine is a toxic compound, but if it was developed with some additives and attached with different chains to be one of the P_{ILs} compounds, it approached pointing truly greener and more secure P_{ILs} to the environment.

Owing to rising environmental regulations, developing nontoxic alternatives compared to hazardous inorganic inhibitors is receiving more attention nowadays. Depending on their specific structural characteristics, they can exhibit diverse biological activities, synergistic effects and versatile applications. So, this paper is concerned with evaluating the action of the newly synthesized P_{ILs} on the electrochemical corrosion processes as anodic dissolution under mass transport control. Depending on its simplicity, the mass transfer coefficient can be obtained using the limiting current technique, which has gained wide acceptance in recent decades. The inhibitors were added with different concentrations at several temperatures to know their inhibition efficiency. Additionally, global quantum chemical descriptors, Fukui indices, local softness, local electrophilicity, dual Fukui function, dual local softness, and dual local philicity were investigated and discussed in more detail to understand the mechanism, the interactions, and the structural orientation of the two PILs and the metallic surface.

Methodology (experimental)

Synthesis of inhibitors molecules

According to our previous work, the desired (P_{ILs}) 1-(2-(4-bromophenyl)-2-oxoethyl)-3-((2-(1-(2-(4-bromophenyl)-2-oxoethyl) pyridine-1-ium-4 carbonyl) hydrazono) methyl) pyridine-1-ium tetrafluoroborate (**BPHP**) and 1-(2-(4-trifluoromethyl phenyl)-2-oxoethyl)-3-((2-(1-(2-(4-trifluoromethylphenyl)-2-oxoethyl) pyridin-1-ium-4-carbonyl) hydrazono) methyl) pyridin-1-ium tetrafluoroborate (**TFPHP**) were prepared by quaternation of the pyridinium nitrogen atom of the generated bis-pyridine derivative[41], followed by a metathesis event (Fig. 1).

Thus, the corresponding PILs **3(a, b)** were produced in good yield by thermally alkylating the initial bis-pyridine hydrazine **1** with two equivalents of 4-substituted-phenacyl bromide **2(a, b)** (Fig. 1). The ^{1}H NMR, ^{13}C NMR, and mass spectra analysis confirmed the synthesis of the intended **3a**. As a result, the two doublets at δ_H 6.67 ppm in the ^{1}H NMR spectrum were assigned to the two new methylene protons (2×$COCH_2$). An extra eight aromatic protons were also recorded at their usual chemical shifts belonging to the two aromatic rings of the phenacyl core. All remaining protons resonated in their respective area. The ^{13}C NMR spectrum of **3a** supported the quaternization reaction, showing the methylene carbons resonating at δ_C 66.67 and 66.73 ppm, respectively.

The displacement of the bromide anion (Br^-) and the furnishing of the desired task-specific PILs **4(a, b)** in good yield were accomplished by treating the synthesized dipyridinium bromide **3(a, b)** with potassium tetrafluoroborate. The success of the anion exchange was unambiguously evidenced by their spectroscopic results, which divulged that there was no change in their ^{1}H and ^{13}C NMR data compared to their corresponding starting pyridinium bromide **3(a, b)**. Correspondingly, the resulting P_{ILs} **4(a, b)** structure was deduced based on their ^{31}P, ^{11}B, ^{19}F NMR, and mass spectra.

The structure of P_{ILs} **4 (a, b)** showed the presence of a multiple resonating between δ_B (−1.64) to (−1.78) ppm in its ^{11}B spectrum and two doublets at δ_F −149.32 and −149.65 ppm in its ^{19}F NMR spectrum respectively, supported the presence of tetrafluoroborate anion (BF_4^-) in the P_{ILs} **4 (a, b)** as counter anion, more spectral data of synthesis were mentioned in the Supplementary figures 1–6.

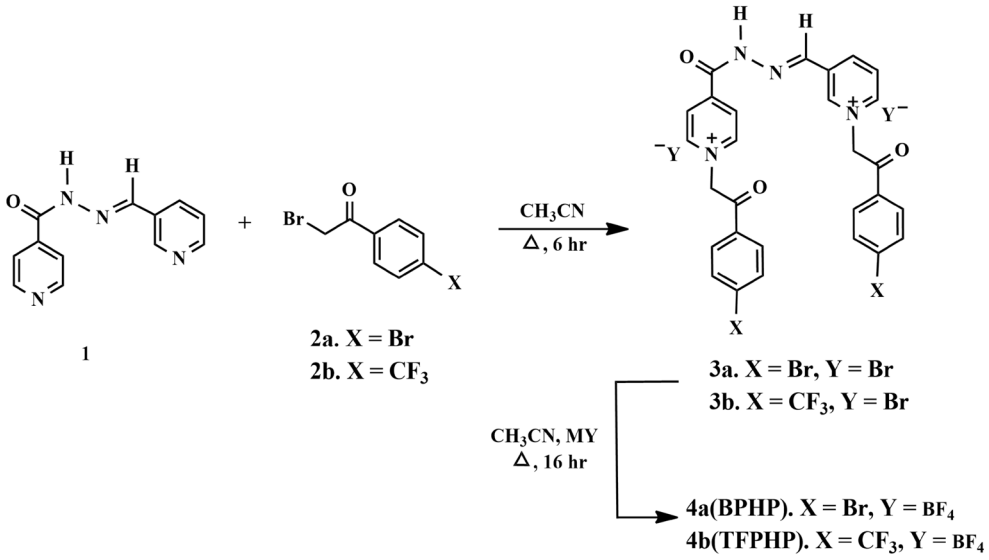

Figure 1. Synthetic routes for synthesizing di-cationic pyridinium ionic liquids **4a–4b.**

Electrode sample and corrosive medium

The corrosive medium, 8 M H_3PO_4, was prepared using analytical grade phosphoric acid (85% w/w) supplied by Fisher Chemicals Ltd. The electrode sample used for electrochemical measurements was carbon steel (CS) having a surface area of 10 cm^2 and the composition (wt.%) was determined by JEOL apparatus JSM-IT200 model: 0.14% Carbon, 0.02% Silicon, 0.56% Manganese, 0.03% Phosphorus, 0.01% Nickel, 0.01% Chrome, 0.01%Vanadium, 0.03% Aluminum, 0.04% Sulfur, and 99.15% Iron. We must be aware that the selection of 8 M H_3PO_4 is based on that the H_3PO_4 concentration effect on the value of limiting current I_{Lim} can be interpreted via the mass transform concept[10,11].

All experiments were carried out using 100 ml of the prepared phosphoric acid in various concentrations of the studied P_{ILs} inhibitors (1.25, 2.5, 7.5, 12.5, 17.5, 25 and 37.5) 10^{-5} M by dissolving in water for **BPHP** and **TFPHP**. The I_{Lim} was recorded for them at different temperatures: 293, 298, 308 and 318 K. Experiments were triple-checked to ensure the measurements were accurate and the results were within 2% error. The reported corrosion data is the average of the three measurements.

Galvano-static polarization measurements

Due to its simplicity and accuracy, the Galvano-static technique may be a common tool to survey inhibitors' inhibition efficiency. Within the present study, standard methods that were described previously were used to perform the polarization experiments[10–13].

Spectroscopic analysis

After corrosion exposure by applying galvanic polarization, several characterizations were applied to CS in 8M H_3PO_4 without (blank) and with P_{ILs} inhibitors.

The quantity of Fe^{2+} was recorded by atomic absorption spectroscopy (AAS) estimated by ANALYTIK JENA CONTRAA 300 AAS to know the amount of iron ions passed into the solution after corrosion measurements and that for environmental protection.

The roughness of the CS surface was shown by atomic force microscope (AFM) Auto probe cp-research head manufactured by Thermomicrpscope operated in contact mode using Silicon Nitride probe model MLCT manufactured by Bruker. Proscan 1.8 software was used for controlling the scan parameters. Scan parameters: (contact mode, scan area 25 × 25 μm^2, scan rate 1 Hz, number of data points 256 × 256 points) and IP 2.1 software for image analysis.

UV–visible reflectance spectroscopy (Jasco V-570) in the 200–700 nm range was used to get the brightness degree and reflection spectra.

Ultraviolet–visible absorption spectrophotometry [*Pg* instruments t-80 UV–Visible spectrophotometer] was used to recognize the absorption of metal and inhibitors in the solution.

Scanning electron microscope (SEM) shows the shielding layer on the CS surface and its morphological characterization. It coupled with the electron disperses X-ray spectroscopy (EDX) analyzer to determine the elemental constituents of layers formed on the corroded surface using a JEOL apparatus JSM-IT200 model.

X-ray photoelectron spectroscopy (XPS) analyses were performed by K-ALPHA (Themo Fischer Scientific, USA) with monochromatic X-ray AL K-alpha radiation (energy – 10 to 1,350 eV) under a vacuum of 10–9 with full-spectrum pass energy 200 eV at narrow-spectrum 50 eV. The analysis spot size was 400 µm in diameter. All binding energy values were determined concerning the C1s line originating from adventitious carbon.

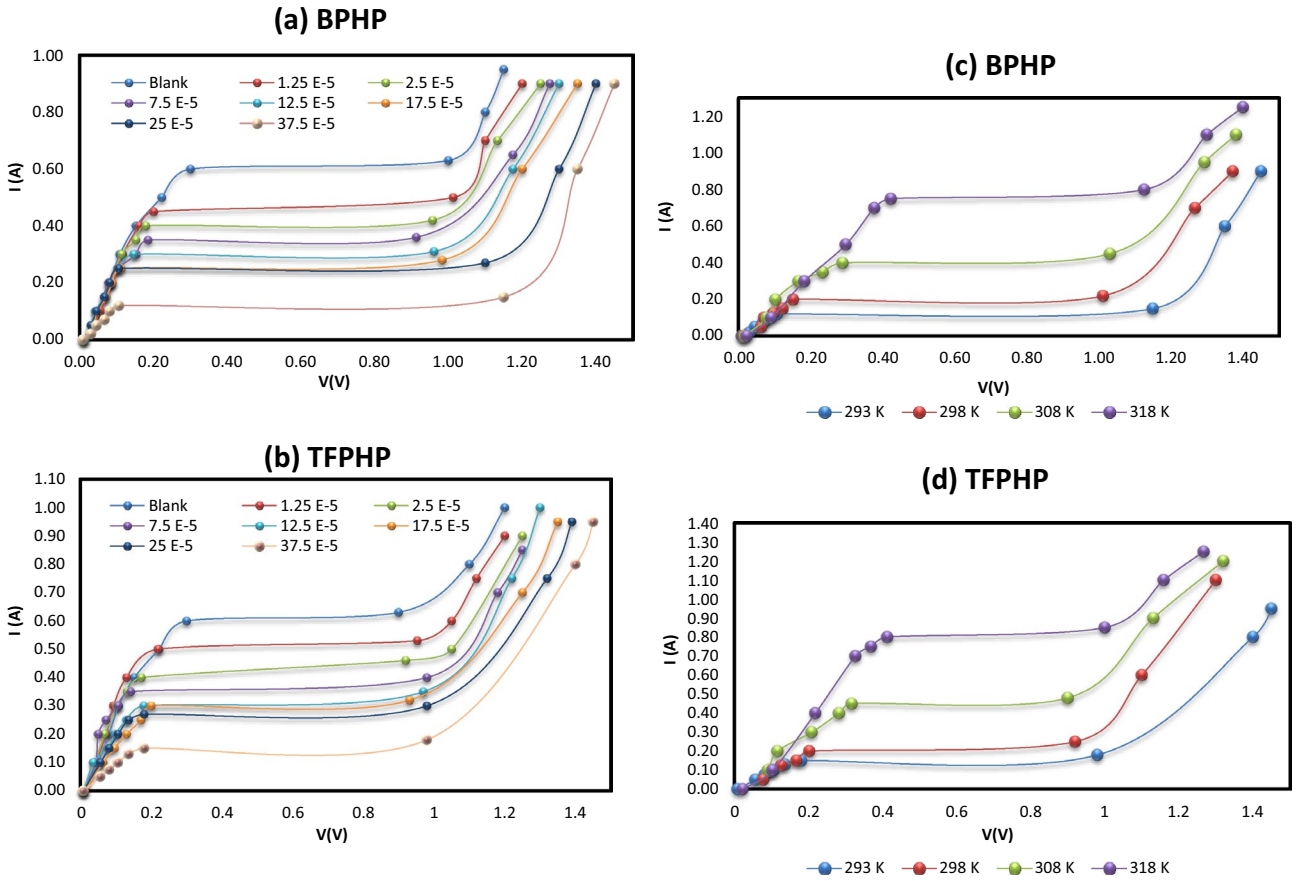

Figure 2. Polarization curves of the tested CS (**a**, **b**) at different P_{ILs} concentrations at 293 K & (**c**, **d**) at different temperatures for P_{ILs} concentration 37.5×10^{-5} M.

Theoretical studies

On the other hand, the theoretical calculations achieved the experimental data using Gaussian-09 with DFT results with method *B3LYP/6-311G (d, p)* showing the structures and electronic properties in the gas and liquid phase.

Results and discussion

Galvanostatic polarization curves

The electrochemical polarization experiments were conducted to understand the kinetics and suppression mechanism the studied PILs inhibitors provided at the CS/H_3PO_4 interface. This goal was provided by the analysis of current–potential curves obtained from Galvanostatic measurements.

It can be seen from Fig. 2 and Table 1 that adding P_{ILs} compounds (**BPHP** & **TFPHP**) significantly reduced the corrosion limiting current values by increasing inhibitor concentrations and enhancements by temperatures compared to the blank curve. P_{ILs} inhibitors block the active sites of the CS surface, indicating that the corrosion of the iron electrode after the adsorption of P_{ILs} was more difficult, and two P_{ILs} showed excellent corrosion resistance. The values of inhibition efficiency ($\%I_{Eff}$) and the degree of the surface coverage was computed by the following Eq. (1)[13,42]:

$$\% = \frac{(I_{Lim}(\text{blank}) - I_{Lim}(\text{ILs})}{I_{Lim}(\text{blank})} \times 100 \quad (1)$$

where I_{Lim}(blank) and $I_{Lim}(P_{ILs})$ are the limiting currents without and with a concentration of inhibitors, respectively. As seen in Table 1, the $\%I_{Eff}$ were enhanced with increasing inhibitor concentration to reach 76.19–71.43% for 37.5×10^{-5} M of **BPHP** and **TFPHP**, respectively. By the way, when adding a higher concentration of the inhibitor than 37.5×10^{-5} M to the solution, the inhibitor would be desorbed from the surface of the metal. Even though, due to the desorption of the inhibitor molecules by increased temperatures, the I_{Eff} of P_{ILs} decrease from 76.19 to 46.20% in the case of temperature variation. This may be attributed to the high dissolution rates of CS at elevated temperatures due to increased solution agitation resulting from the high rate of H_2 gas evolution. This may also reduce the ability of inhibitors to be adsorbed on the CS surface. The results tabulated indicate that the investigated molecules work by adhering to the CS surface and assisting in forming an inhibitory layer that serves as a barrier between the CS surface and the corrosive media's constituent parts. Since **BPHP** has a bigger I_{Eff} than **TFPHP** and a lower desorption rate than **TFPHP**; it is a better inhibitor than the other one (Fig. 3).

P_{ILs}	$C_{PILs} \times 10^5$ (M)	293 K		298 K		308 K		318 K	
		I_{lim}	% I_{Eff}	I_{lim}	% I_{Eff}	I_{lim}	% I_{Eff}	I_{lim}	% I_{Eff}
BPHP	Blank	0.63	0.00	0.74	0.00	1.03	0.00	1.58	0.00
	1.25	0.50	20.63	0.62	16.22	0.90	12.62	1.44	8.86
	2.50	0.42	33.33	0.55	25.68	0.80	22.33	1.27	19.62
	7.50	0.36	42.86	0.47	36.49	0.69	33.01	1.10	30.38
	12.50	0.31	50.79	0.41	44.59	0.61	40.78	0.97	38.61
	17.50	0.28	55.55	0.37	50.00	0.56	45.63	0.89	43.67
	25.00	0.27	57.14	0.34	54.05	0.51	50.48	0.83	47.47
	37.50	0.15	76.19	0.22	70.27	0.45	56.31	0.80	49.37
TFPHP	Blank	0.63	0.00	0.74	0.00	1.03	0.00	1.58	0.00
	1.25	0.53	15.87	0.64	13.51	0.91	11.64	1.47	6.96
	2.50	0.46	26.98	0.57	22.97	0.81	21.36	1.34	15.19
	7.50	0.40	36.51	0.49	33.78	0.73	29.12	1.21	23.42
	12.50	0.35	44.44	0.43	41.89	0.64	37.86	1.06	32.91
	17.50	0.32	49.21	0.39	47.30	0.57	44.66	0.96	39.24
	25.00	0.30	52.38	0.36	51.35	0.54	47.57	0.92	41.77
	37.50	0.18	71.43	0.25	66.22	0.48	53.40	0.85	46.20

Table 1. Limiting current (I_{lim}) values and inhibition efficiency (%I_{Eff}) with and without P_{ILs} at different temperatures and concentrations.

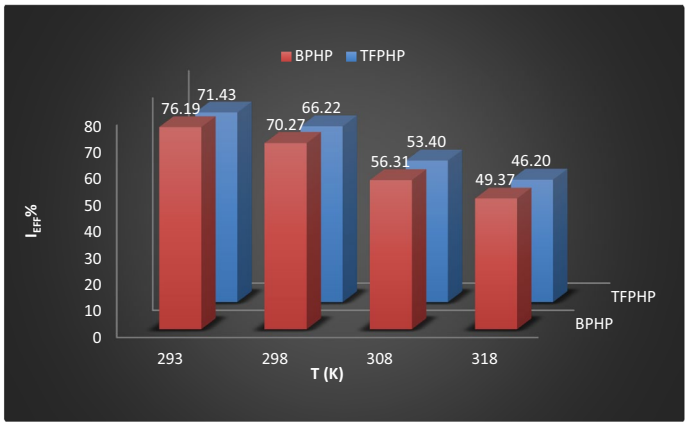

Figure 3. The effect of temperature on the inhibition efficiency (%I_{Eff}) at constant concentration (37.5×10^{-5} M) of P_{ILs}.

Adsorption isotherm behavior and thermodynamics parameters

It would be precious to make sense of the adsorption processing by a fitting adsorption isotherm, which could give further helpful bits of knowledge into the association of the inhibitor with the metal surface and, subsequently, the system of corrosion restraint. To decide the best adsorption isotherm model, which improves the degree of surface coverage area (θ) upon the CS surface. As could be seen, the formation of a defensive layer over the metallic surface, which reduces the reactive surface area for corrosive ion adhesion and hence mitigates corrosion, was shown as the inhibitor quantity was increased by the increase in the θ across the CS substrate. The direct types of considered adsorption isotherm models are as the following: Langmuir, El-Awady and Flory–Huggins applied for the studied P_{ILs} (**BPHP** &**TFPHP**), were determined at 298 K for different concentrations. The direct types of considered adsorption isotherms are described in Table 2, where θ = surface coverage = I_{Eff}%, $C_{P_{ILs}}$ is the P_{ILs} concentration, y is the number of inhibitor molecules involving one dynamic site, x is the number of water atoms supplanted by one particle of the inhibitor, and K_{ads} is the constant of equilibrium of the adsorption interaction, which is temperature dependent. It is related to the free energy of adsorption according to Eq. (2):

$$\Delta G_{ads} = -RTln\,(55.5\,K_{ads}) \tag{2}$$

R, T, and 55.5 M are the ideal gas constant, work temperature (293–318 K), and water content, respectively. Figure 4 shows the linear fit according to the curve derived from the Galvanostatic technique. The adsorption parameters deduced from these isotherms and values of the determination coefficient (R^2) are regrouped in Table 2.

Isotherm model	Linear form	Plot	Parameters	Inhibitors	
				BPHP	TFPHP
Langmuir	$\frac{C_{P_{ILs}}}{\theta}=\frac{1}{K_{ads}}+C_{P_{ILs}}$	$\frac{C_{P_{ILs}}}{\theta}$ vs $C_{P_{ILs}}$	Slope	1.31	1.36
			R^2	0.9578	0.9623
El-Awady	$\log\left(\frac{\theta}{1-\theta}\right)=\log K'+y\log C_{P_{ILs}}$ $(K=K'^{\frac{1}{y}})$	$\log\left(\frac{\theta}{1-\theta}\right)vs\log C_{P_{ILs}}$	R^2	0.9663	0.9779
			y	0.68	0.68
			1/y	1.47	1.48
			K′	402.90	337.36
			K_{ads}	6921.69	5451.00
			ΔG_{ads} (kJ/mol)	−31.86	−31.27
Flory–Huggins	$\log\left(\frac{\theta}{C_{P_{ILs}}}\right)=\log xK_{ads}+x\log(1-\theta)$	$\log\left(\frac{\theta}{C_{P_{ILs}}}\right)vs\log(1-\theta)$	R^2	0.9838	0.9823
			x	3.05	2.98
			K_{ads}	4673.35	4170.24
			ΔG_{ads} (kJ/mol)	−30.89	−30.60

Table 2. Linear isotherm equations and adsorption parameters for P_{ILs} at 298 K.

Figure 4a represents Langmuir's adsorption relationship with linear correlation coefficient (R^2) values approaching one. The outcomes indicate that the Langmuir model displays the best linear relationship, but the slope deviates markedly from unity for **BPHP** and **TFPHP**[43,44]. Besides, the Langmuir model did not achieve; it remains hypothetical and often referred to as ideal adsorption, which is not really applicable in concrete complex electrochemical systems. Electrochemical systems are often referred to as either ideal or non–ideal adsorptions because of the different assumptions on which each adsorption isotherm is based. So, we were obliged to test other isotherm models, namely El–Awady and Flory–Huggins.

It should be pointed out that El–Awady and Flory–Huggin's isotherm can be used to examine the number of water molecules that can be replaced by one inhibitor molecule on the CS surface.

As shown in Fig. 4b, the linear form of Flory Huggins adsorption isotherm as $\log \theta/C_{PILs}$ vs $\log (1-\theta)$ at 298 K. The obtained data reported in Table 2 yielded a linear correlation coefficient (R^2) with slope (x) and intercept (xK). We found that the calculated values of (x) were higher than unity, implying that one **BPHP** and **TFPHP** molecule replaces more than a water molecule at a constant temperature.

On the other hand, the curve fitting of the El-Awady model is shown in Fig. 4c, d at different temperatures, and the calculated values of *K, K′* and *1/y* are listed in Table 3. The strong correlations confirm the validity of the approach. The values of *1/y* ensure that every molecule in the adsorbent mechanism is linked to greater than one active site on the CS outermost layer. It is confirmed that the corrosion inhibitor forms a dense multilayer physisorption of P_{ILs} molecules on the CS surface.

Table 2 shows that the values of K_{ads} obtained from the El-Awady model were large compared to Flory Huggins's adsorption isotherm. In addition, the large value of K_{ads} indicates the high adsorptive power of **BPHP**. On the other hand, Table 3 shows the high values of K_{ads} observed at low temperatures mean that strong interactions of the P_{ILs} molecules with the *Fe* were favored at this temperature.

The free energy of adsorption (ΔG_{ads}) values are assigned from K_{ads} values of the El-Awady adsorption model, which showed the best correlation with the experimental data. The computed values of ΔG_{ads} for the P_{ILs} compounds at various temperatures are recorded in Table 3. Negative signs of ΔG_{ads} elucidate the spontaneous adsorption of the studied P_{ILs} on the CS surface [45]. The ΔG_{ads} values range from −32.13 to −31.78 kJ.mol^{-1} for **BPHP** and from −31.37 to −31.09 kJ. mol^{-1} for **TFPHP,** clarifying that the P_{ILs} adsorption process in 8M H_3PO_4 involves both physisorption and chemisorption mechanisms (physicochemical), which signifies a complex mode between CS and inhibitor molecules[46–49]. In another way, physicochemical meaning involves electrostatic interactions between the charged molecules and the metal (physisorption) and also sharing or transfer of electron pairs or π electrons from organic molecules to the metal surface to form a coordinate bond (chemisorption).

Else important thermodynamic parameters are obtained by Vant't Hoff equation, which is utilized to assess enthalpy of adsorption (ΔH_{ads}) by plotting lnK_{ads} vs *1/T*. A linear relation is gained with a slope equal to ($-\Delta H_{ads}$) /*R*). The values of (ΔH_{ads}) were computed and registered in Table 3. The negative amount of ΔH_{ads} shows that the adsorption of the inhibitor is an exothermic interaction; this outcome might make sense of how the adsorption is consistent, and afterward, the inhibition decreases with expanding temperature. In this work, the values of ΔH_{ads} for the adsorption of the inhibitor are − 35.46 kJ/mol for **BPHP** and −34.33 kJ/mol for **TFPHP**. This value is closer to − 40 kJmol^{-1} and far from − 100 kJmol^{-1}. It implies that the adsorption of P_{ILs} follows physicochemical[50]. The Gibbs–Helmholtz equation is utilized to deduce the standard entropy of the adsorption ($\Delta°S_{ads}$) at 298 K according to the following Eqs. (3) and (4):

$$lnK_{ads} = \left(\frac{-\Delta H_{ads}}{RT}\right) + Constant \tag{3}$$

$$\Delta G^{\circ}_{ads} = \Delta H^{\circ}_{ads} - T\Delta S^{\circ}_{ads} \tag{4}$$

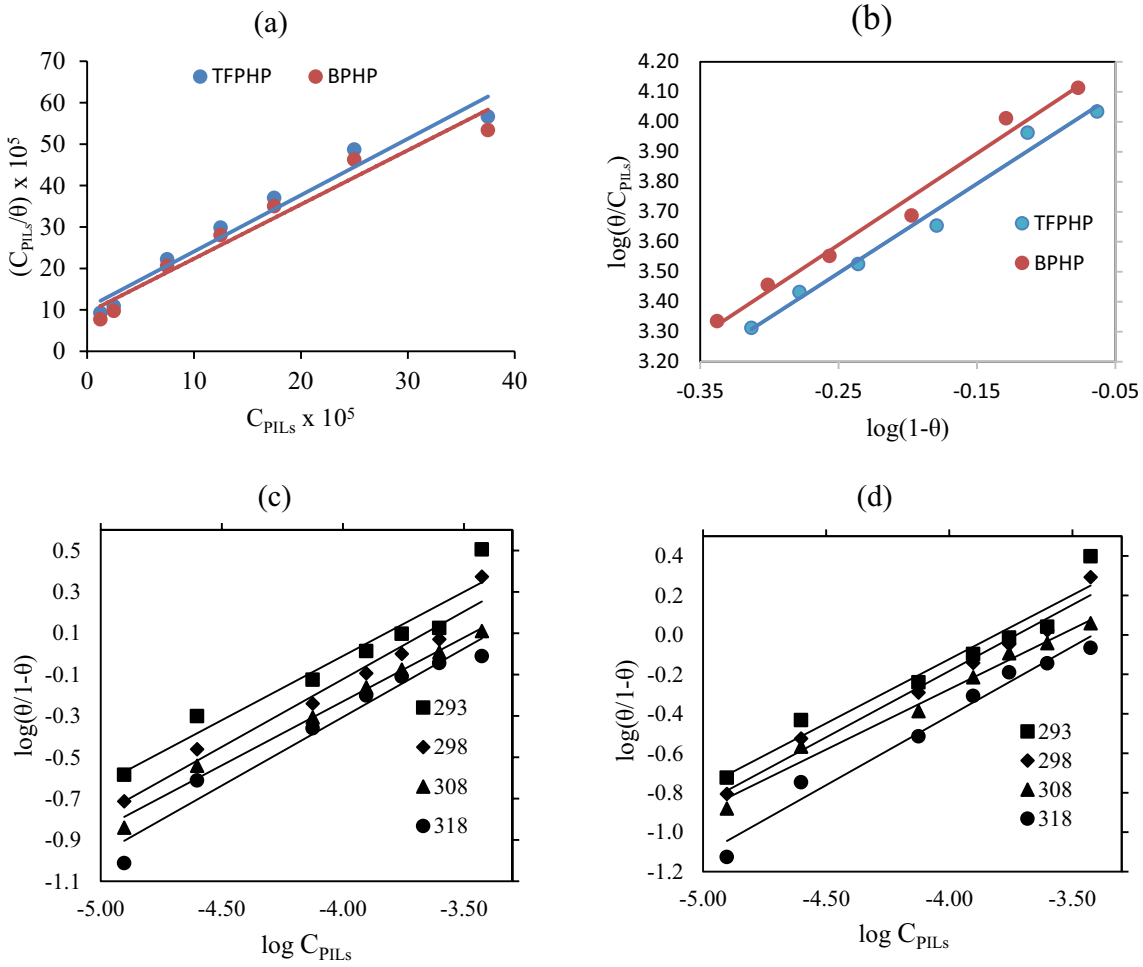

Figure 4. P_{ILs} adsorption isotherm models for CS tested electrodes in 8 M H_3PO_4 with different concentrations for isotherm equations in Table 2 (**a**) Langmuir model by plotting (**b**) Flory–Huggin's model. Elawady model (**c**) **BPHP** (**d**) **TFPHP.**

The negativity of adsorption entropy $\Delta S°_{ads}$, obtained in this work, suggests a reduction in the translational degrees of freedom and perturbation, possibly due to the accumulation of water molecules on the surface.

The active thermodynamic model used for driving the heat of adsorption (Q_{ads}) for extra increased understanding of the adsorption procedure using Eq. (5)[51]:

$$\log\left(\frac{\theta}{1-\theta}\right) = \log A + \log C_{P_{ILs}} - \left(\frac{Q_{ads}}{2.303RT}\right) \tag{5}$$

where A is a constant and $C_{P_{ILs}}$ is the concentration of inhibitors, Fig. 5 shows the relation between $log\left(\frac{\theta}{1-\theta}\right)$ with $\frac{1000}{T}$, the slope equals $-(\frac{Q}{2.303R})$. For the **BPHP** (Q_{ads} = − 28.872 kJ/mol) and **TFPHP** (Q_{ads} = − 27.349 kJ/mol). The negative value of Q_{ads} shows that the surface coverage level diminishes with a temperature rise in the

P_{ILs}	BPHP							TFPHP						
T (K)	y	1/y	K'	K_{ads}	ΔG_{ads} (kJ/mol)	ΔH_{ads} (KJ/mol)	$\Delta S°_{ads}$ (J/mol.K)	y	1/y	K'	K_{ads}	ΔG_{ads} (kJ/mol)	ΔH_{ads} (KJ/mol)	$\Delta S°_{ads}$ (J/mol.K)
293	0.62	1.61	297.17	9628.71	−32.13	−35.46	−12.08	0.68	1.47	422.28	7049.53	−31.37	−34.33	−10.29
298	0.68	1.47	402.90	6921.69	−31.86			0.68	1.48	337.36	5451.00	−31.27		
308	0.64	1.57	211.88	4495.68	−31.82			0.61	1.64	147.67	3541.99	−31.21		
318	0.51	1.97	58.36	2996.22	−31.78			0.61	1.64	112.07	2307.51	-31.09		

Table 3. Thermodynamic parameters data of P_{ILs} by ELAwady adsorption model.

presence of inhibitors and exothermic processes[52,53]. The higher absolute value of **BPHP** means that its molecules were adsorbed more than **TFPHP**.

To recognize physisorption and chemisorption, the isotherm of Dubinin-Radushkevich has been utilized and described as follows[54]:

$$\ln\theta = \ln\theta_{\max} - a\delta^2 \tag{6}$$

where θ_{max} is the maximum surface coverage, and δ is the Polanyi potential described by:

$$\delta = RTln\left(1 + \frac{1}{C_{P_{ILs}}}\right) \tag{7}$$

By plotting *ln θ* against δ^2 Fig. 6, the constant *a* was obtained from the slope. The values of *a* prompt the mean adsorption energy E_m for the different temperatures are in Table 4 This energy, which is the exchange energy of 1 mol of adsorbate from the solution bulk to the outer layer of the adsorbent, is characterized as:

$$E_m = \frac{1}{\sqrt{2a}} \tag{8}$$

The extent of E_m gives data about the kind of adsorption type to be chemisorption or physisorption: E_m values under 8 kJmol^{-1} demonstrate physical adsorption, while those higher than 8 kJmol^{-1} recommend chemisorption, so the E_m values mean physical adsorption for the two inhibitors[54–57].

Kinetic parameters

The kinetic model was another helpful tool for making sense of the erosion resistance and further explaining the inhibitors' features. The activation energy values E_a were evaluated via the linearized form of the Arrhenius equation with a temperature range of (293–318 K) for CS disintegration in the absence and presence of **BPHP** and **TFPHP** as follows:

$$lnI_{Lim} = lnAE_a/RT \tag{9}$$

The linear regression plots between ln I_{Lim} versus 1000/T are presented in Fig. 7; the values of E_a (energy of activation) are derived from the slopes = (− E_a/R) where gas constant R = 8.314 JK^{-1} mol^{-1} and A is that the factor of frequency. The calculated data at different inhibitor concentrations were collected in Table 5. The change in the values of the apparent activation energies may be explained by the corrosion process's mechanism alterations in the presence of adsorbed P_{ILs} inhibitor molecules.

It was observed that E_a for the uninhibited solution is lower than that of the inhibited solution, supposing that the dissolution of CS is slow within the existence of P_{ILs} inhibitors. The inhibitor is adsorbed on the most active adsorption sites (having the lowest energy), and the corrosion process takes place predominantly on the active sites of higher energy. Inspection of the data shows that E_a values increase in the presence of the **BPHP** or **TFPHP** [46,58,59], and the values of **TFPHP** were smaller than **BPHP**. This indicates that the energy barrier between the reactants and the activated complex depends on the chemical composition of the inhibitor. Because of the expanded energy hindrance for metal dissolving, this information demonstrates how the inhibitors can restrict consumption. The creation of a coating layer covering the surface goes about as an energy, furthermore, mass exchange boundary, raising the activation energy.

The enthalpy $\Delta H^{\neq}$ and entropy $\Delta S^{\neq}$ of activation were frequently determined by utilizing the substitutional recipe of the Arrhenius equation, change state condition as follows:

$$Ln\,(I_{Lim}/T) = ln(R/Nh) + (\Delta S^{\neq}/R)(\Delta H^{\neq}/RT) \tag{10}$$

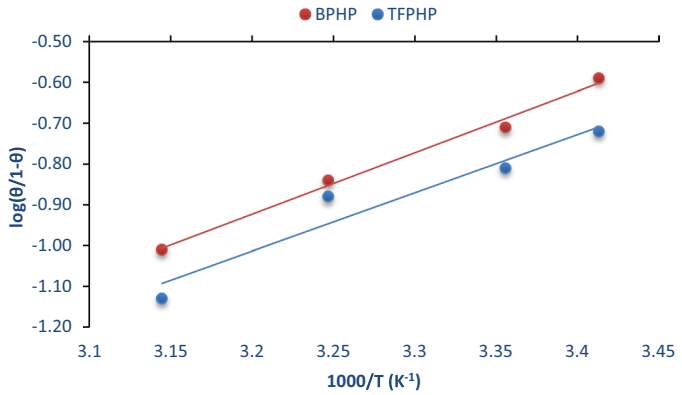

Figure 5. The active thermodynamic model used for driving the heat of adsorption (Q_{ads}).

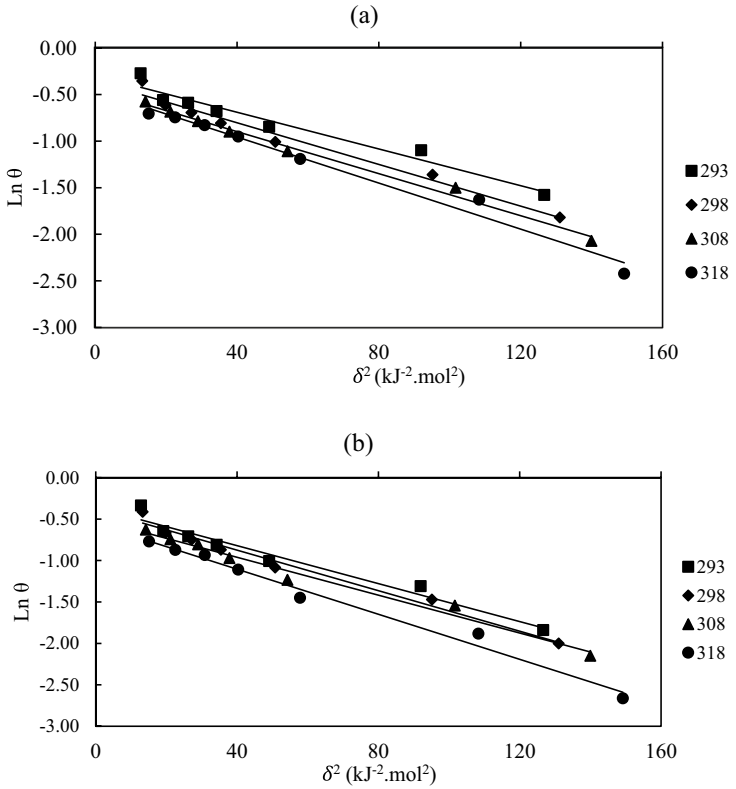

Figure 6. Dubinin-Radushkevich isotherm to recognize physical or chemical adsorption (**a**) **BPHP** (**b**) **TFPHP.**

P_{ILs}	T (K)	R^2	a (kJ^{-2} mol^2)	θ_{max}	E_m ($kJmol^{-1}$)
BPHP	293	0.9563	0.0099	0.74378	7.1066905
	298	0.9734	0.0112	0.70082	6.681531
	308	0.9912	0.0113	0.63979	6.65190
	318	0.9797	0.0124	0.63027	6.35001
TFPHP	293	0.9604	0.0115	0.69607	6.59380
	298	0.9796	0.0122	0.67997	6.40184
	308	0.9815	0.0114	0.60429	6.62266
	318	0.9854	0.0136	0.57103	6.06339

Table 4. Data of Dubinin-Radushkevich adsorption energy isotherm to recognize physical or chemical adsorption.

where h is Planck's constant, N is Avogadro's number, and T is the temperature. From Table 5, the E_a and $\Delta H^{\neq}$ values shifted similarly, allowing us to confirm the known thermodynamic response between the E_a and $\Delta H^{\neq}$ as Eq. (11), which is equivalent to the average value of RT (2. 53 kJ/mol) at the average temperature (308 K) of the domain investigation.

$$E_a - H^{\neq} = RT \tag{11}$$

$\Delta H^{\neq}$ positive values show that forming the activated complex is an endothermic process. $\Delta S^{\neq}$ values can be determined from the intercepts (equal to $ln\ (R/Nh) + (\Delta S^{\neq}/R)$). The negative $\Delta S^{\neq}$ values of the inhibitors indicated that the activated complex within the rate-determining step addresses association rather than dissociation. This means that increasing ordering occurs on going from reactants to activate complex, and this may result from the P_{ILs} inhibitor molecules' adsorption from the acidic solution and may be viewed as a quasi-substitution process between the water molecules at the CS electrode and the P_{ILs} substance in the aqueous phase. The change in free energy activation ($\Delta G^{\neq}$) was determined from the Arrhenius with the Eq. (12):

$$\Delta G^{\neq} = \Delta H^{\neq} - TS^{\neq} \tag{12}$$

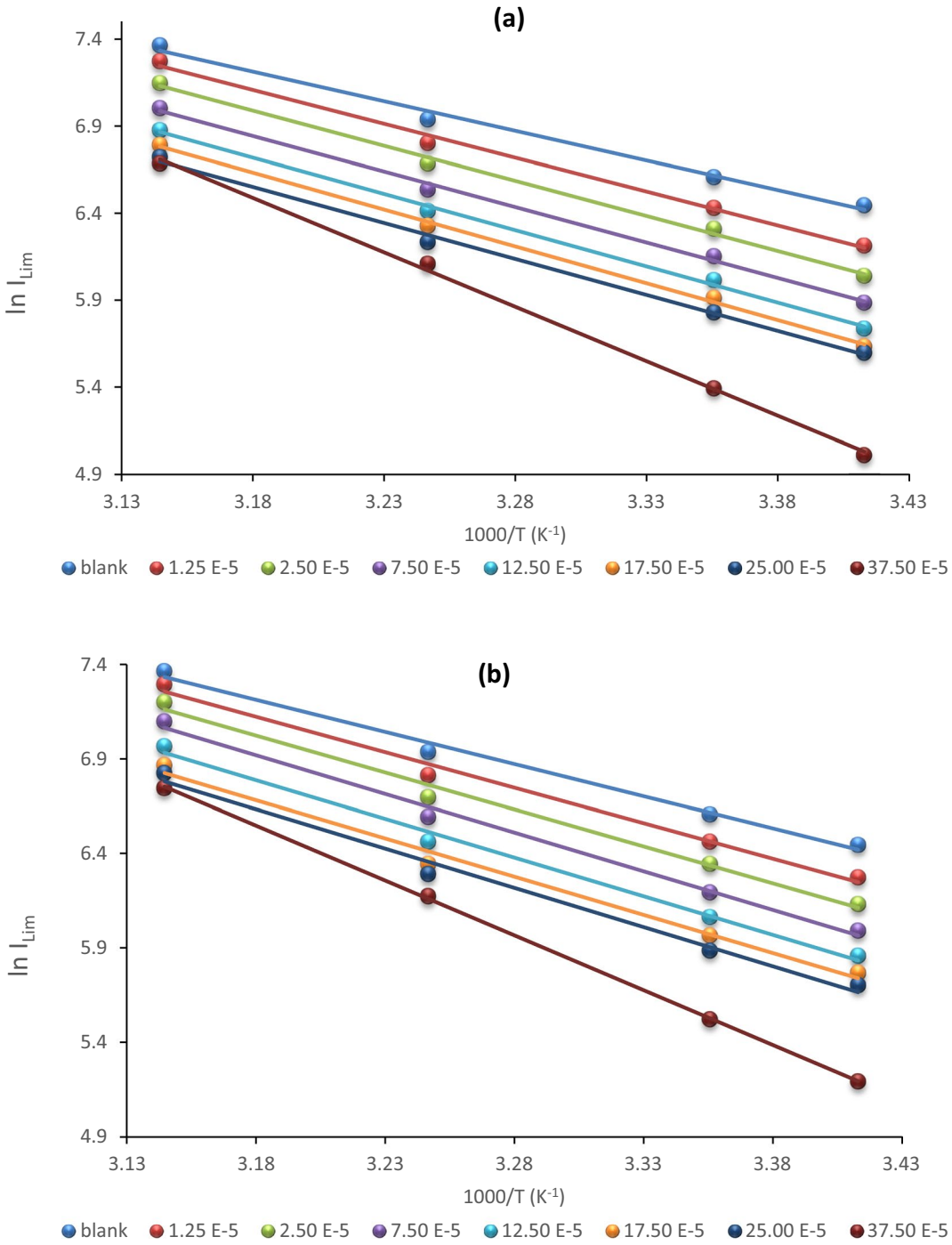

Figure 7. Arrhenius graphs for determination energy of activation from the relation between limiting current and temperature with and without P_{ILs} (**a**) **BPHP** (**b**) **TFPHP.**

$\Delta G^{\neq}$ values are positive, increasing in the inhibited case more than in the blank case[10,60,61].

Atomic absorption spectroscopy measurements (AAS)

AAS is a sensitive, relatively affordable, spectrometric element-selective detector, making it ideal for determining a wide range of elements at trace and ultra-trace levels. Additionally, based on the solubility of the corrosion products, it is a powerful analytical approach used to forecast the corrosion rate in various media, including acidic, basic, and neutral media. Based on the amounts of iron (Fe^{2+}) in the protected and unprotected systems, the absorbance percentage inhibition efficiency ($\%€AAS$) of the P_{ILs} on the CS surface in 8M H_3PO_4 solution was obtained using Eq. (13)[61]. According to the AAS data in Table 6, solutions with **BPHP** inhibitor have lower concentrations of (Fe^{2+}) as the temperature drops or the concentration rises than solutions without inhibitor.

P_{ILs}	$C_{PILs} \times 10^5$ M	E_a kJ/ mol	$\Delta S^{\neq}$ J/mol.K	$\Delta H^{\neq}$ kJ/mol	$\Delta G^{\neq}$ kJ/mol	Ea-$\Delta H^{\neq}$ kJ/mol
BPHP	Blank	28.28	−85.36	25.75	57.24	2.53
	1.25	32.34	−106.61	29.81	62.46	2.53
	2.50	33.51	−158.03	30.98	79.06	2.53
	7.50	33.90	−88.71	31.37	58.36	2.53
	12.50	34.63	−87.41	32.10	58.70	2.53
	17.50	35.23	−86.23	32.70	58.93	2.53
	25.00	34.41	−89.50	31.88	58.11	2.53
	37.50	52.06	−33.89	49.53	59.84	2.53
TFPHP	Blank	28.28	−85.36	25.75	57.24	2.53
	1.25	31.21	−109.21	28.68	62.11	2.53
	2.50	32.49	−158.03	29.96	78.19	2.53
	7.50	34.01	−87.70	31.48	58.17	2.53
	12.50	34.03	−88.76	31.50	58.50	2.53
	17.50	33.64	−90.87	31.11	58.76	2.53
	25.00	34.55	−88.37	32.02	58.91	2.53
	37.50	48.30	−45.37	45.77	59.57	2.53

Table 5. The activation parameters values E_a, $\Delta H^{\neq}$, $\Delta S^{\neq}$ *and* $\Delta G^{\neq}$ with and without P_{ILs} of different concentrations in 8 M H_3PO_4.

BPHP inhibitor has lower ions of (Fe^{2+}) because it is more effective at inhibiting corrosion than **TFPHP**[62]. Therefore, inhibitors have a strong indication for inhibiting the corrosion of CS.

$$\%€AAS = \left(1 - \frac{C_{inh}}{C_{blank}}\right) \times 100 \tag{13}$$

where C_{blank} and C_{inh} are (Fe^{2+}) ions concentrations in the absence and presence of the P_{ILs} inhibitors.

UV–visible analysis

To demonstrate how a complex form, UV–VIS analysis was used with the metal cations (Fe^{2+}) and P_{ILs} under study. Without adding any inhibitor, the CS electrode was subjected to the corrosive 8 M H_3PO_4 electrolyte at 293 K (**Blank**). The two PILs were also dissolved at a high molar concentration (37.5×10^{-5} M) in the same corrosive electrolyte used for the blank sample (**solution A = P_{IL} + 8 M H_3PO_4**). In addition, a different solution (**solution B = P_{IL} + CS + 8 M H_3PO_4**) contained a CS electrode and a predetermined molar concentration of P_{ILs} (37.5×10^{-5} M) dissolved and submerged once more in the same corrosive electrolyte (8 M H_3PO_4) at 293 K. For each P_{ILs} inhibitor, the UV was measured for the three different solutions [11], and the absorption wavelengths were noted and demonstrated in Fig. 8. The resulting wavelengths for the blank solution were 225, and 300 nm, which could be attributed to π–π*(*C* = *C*) and n–π* (C = O) transition, respectively. While in the case of solution A, the observed absorption values for the C=C bond due to (π–π*) were 235 nm, and the C=O bond due to (n–π*) was 310 nm for **TFPHP**. For **BPHP**, recorded high absorbance (hypochromic shift) at 240 and 320 nm is employed for C=C (π–π*) and C=O (n–π*), respectively. Additionally, for solution B, the absorption peak values were

Samples	[Fe^{2+}] (mg L^{-1})	Signal absorbance	%€AAS
Iron + 8 M H_3PO_4 (293 K)	109.30	0.65700	–
Iron + 8 M H_3PO_4 (298 K)	110.10	0.69018	–
Iron + 8 M H_3PO_4 (308 K)	121.50	0.85700	–
Iron + 8 M H_3PO_4 (318 K)	124.90	1.18630	–
Iron + 8 M H_3PO_4 + 37.5×10^{-5} M BPHP (293 K)	27.36	0.19900	74.97
Iron + 8 M H_3PO_4 + 37.5×10^{-5} M TFPHP (293 K)	33.26	0.33560	69.57
Iron + 8 M H_3PO_4 + 1.25×10^{-5} M BPHP (293 K)	87.41	0.43050	20.03
Iron + 8 M H_3PO_4 + 37.5×10^{-5} M BPHP (293 K)	27.36	0.19900	74.97
Iron + 8 M H_3PO_4 + 37.5×10^{-5} M BPHP (293 K)	27.36	0.19900	74.97
Iron + 8 M H_3PO_4 + 37.5×10^{-5} M BPHP (298 K)	53.35	0.40223	51.54
Iron + 8 M H_3PO_4 + 37.5×10^{-5} M BPHP (308 K)	73.80	0.45400	39.26
Iron + 8 M H_3PO_4 + 37.5×10^{-5} M BPHP (318 K)	89.60	0.72400	28.26

Table 6. Atomic absorption spectroscopy data shows the effect of P_{ILs} with different concentrations and temperatures on iron ions and the absorbance percentage inhibition efficiency (*%€AAS*).

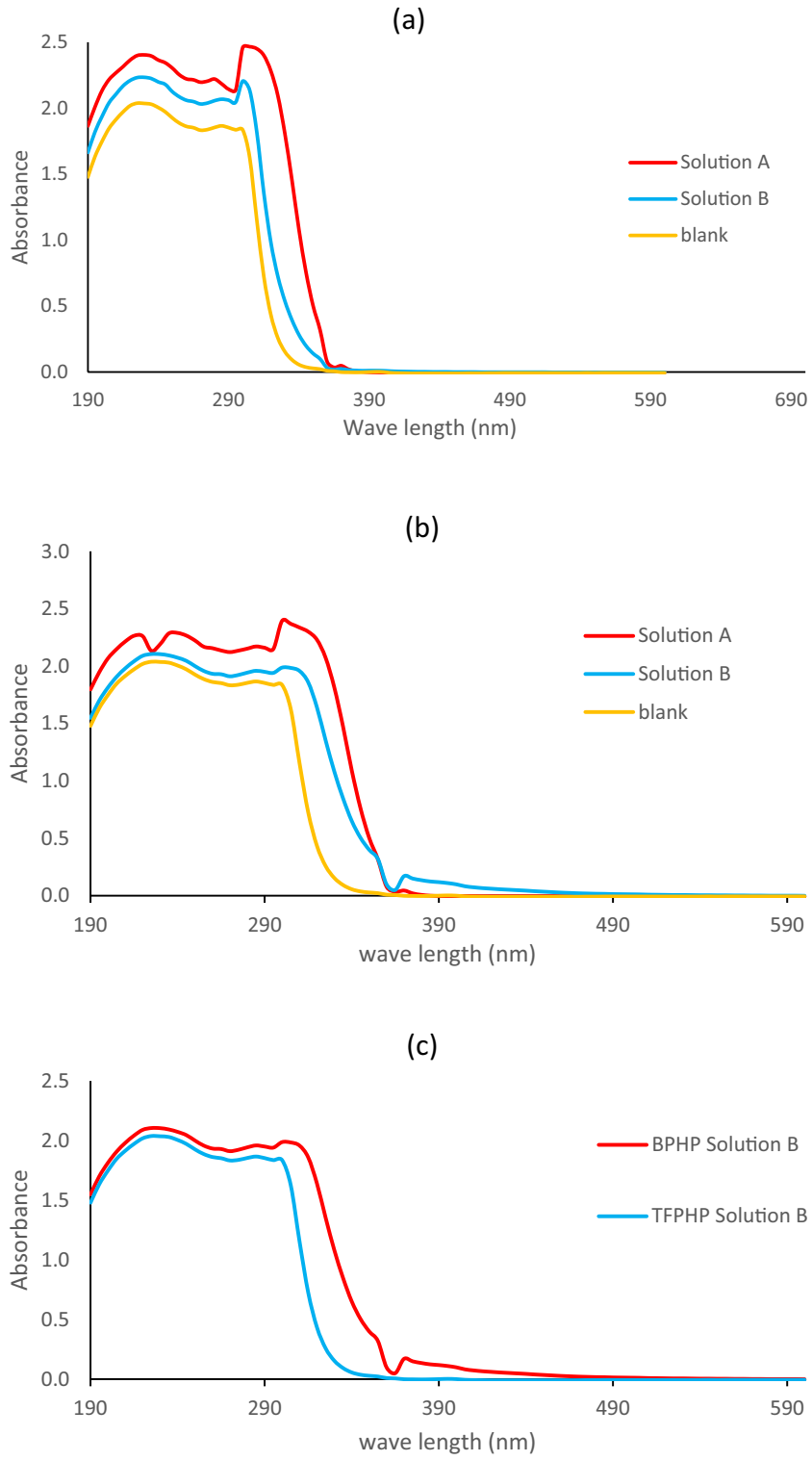

Figure 8. Spectra of uv–visible comparison at same concentration 37.5×10^{-5} M and temperature 293 K. (**a**) **TFPHP** before and after immersing in CS with blank. (**b**) **BPHP** before and after immersing in CS with blank. (**c**) **BPHP** and **TFPHP** after corrosion.

changed and shifted to 230 nm for C=C (π–π*), 305 nm for C=O (n–π*) in the case of **TFPHP**, and for **BPHP,** the absorption values appeared at 235 nm for C=C (π–π*) and for 310 nm C=O (n–π*) (bathochromic shift)[63]. Moreover, the results mentioned above reveal an important distinction in the absorption peaks in Fig. 8 between

BPHP and **TFPHP**, suggesting that **BPHP** is the most effective inhibitor. This spectroscopic method provides proof of the complex formation between P_{ILs} inhibitors and metallic electrodes[64].

SEM and EDX spectroscopy

To support the results mentioned above, films on CS surfaces were examined using an SEM–EDX study after exposure to aggressive acidic media. The distinct elements present on the CS surface of each film can be identified using the EDX technique, as can the elemental changes that resulted during immersion in 8M H_3PO_4 solution free of and with P_{ILs} under various concentrations and temperatures[65,66]. The results of the EDX spectra in Fig. 9 demonstrate that the key elements of the existence of the element on the CS surface are shown by the solution-free inhibitor (blank). It is also observed in Table 7 that the percentage atomic content of *O* and *P* remarkably reduced by changing inhibitor and temperature due to CS surface coverage by a homogeneous adsorbed film. Additionally, the surface characterization of CS samples (×5000), where the surface was highly destroyed under inhibitor-free conditions, confirmed the adsorption of P_{ILs}. After the adsorption of P_{ILs}, By the way, the hetero atoms such as *C* and *O* indicate that at the active sites of adsorption, the surface becomes smoother when the percent of *Fe* and *C* increase, *O* and *P* decrease with increasing inhibition of the corrosion. The inhibition and the surface smoothing, as observed from SEM Fig. 9, are directly probational with increasing the concentration; the least smoothing surface is blank (%*Fe* = 37.32, %*C* = 1.21, %*O* = 54.81 and %*P* = 15.66) and for 1.25×10^{-5} M (%*Fe* = 47.29, %*C* = 3.51, %*O* = 33.13 and %*P* = 8.93) is less smooth than 3.75×10^{-4} M (%*Fe* = 62.66, %*C* = 3.34, %*O* = 21.55 and %*P* = 5.29) at same temperature 293 K for **BPHP** and the same competition for **TFPHP**. As the temperature increases at 37.5×10^{-5} M, the inhibition decreases at 318 K (%*Fe* = 52.28), more than 293 K (%*Fe* = 62.66) for **BPHP**.

On the other hand, **BPHP** has more inhibition than **TFPHP** at the same concentration and temperature because **BPHP** forms more surface coating than **TFPHP**. However, it can be noticed from EDX recorded in the presence of P_{ILs} in Fig. 9 the appearance of new peaks related to the *N* atom, which act as active centers of these inhibitors for adsorption and forming a protected film on the CS surface. On the other hand, Br appeared on the EDX diagram for **BPHP** due to the difference between two structures: the terminal group, *Br*, for **BPHP** and CF_3 group for **TFPHP** and the group BF_4^- the negative ion for both inhibitors where *F* appeared in the EDX.

Atomic force microscopy (AFM)

Presently, several imaging techniques are now available that can provide accurate three-dimensional topographies and information about the irregularities on the sample surface. One uses an AFM to provide quantitative analysis rather than SEM micrographs' qualitative analysis[67]. Figure 10a–f illustrates the 2D and 3D morphological characteristics of CS surfaces immersed in 8 M H_3PO_4 at various temperatures and concentrations with and without P_{ILs} inhibitor **BPHP** or **TFPHP**. Table 8 lists the values for the average surface roughness (*Ra*), which reflects the deviation in height, the root means square roughness (*Rq*), which represents the deviation in surface heights, and the maximum peak to valley depth (*Rp-v*).

The P_{ILs} layer on the CS surface in solution-free inhibitors is shown in Fig. 10. Direct contact with 8M H_3PO_4 media totally damages the corroded CS surface with an average roughness (*Ra*) of 0.62 µm, *Rq* of 0.79 µm, and *Rp-v* of 5.00 µm. On the other hand, as the inhibition increased, the parameters roughness decreased[68], resulting in an improvement of the surface quality film and the formation of a more uniform film that was observed by adding the optimum concentration of **TFPHP** (37.5×10^{-5} M) at 293 K. These parameters roughness magnitude decreased to *Ra* of 0.18 µm, *Rq* of 0.25 µm, and *Rp-v* of 2.31 µm. This coating is a barrier between the metal and the corrosive medium and considerably prevents CS deterioration. However, the surface roughness parameters decreased in the presence of **BPHP** Fig. 11, owing to the more protective activity of adsorbed inhibitor molecules on the CS surface rather than **TFPHP**, as evidenced by a decrease in average surface roughness values. Table 8 shows the percent inhibition ($\%I_{Eff}$) increased with increasing the concentration and decreasing the temperature for **BPHP**. By comparing the parameters, the values of **BPHP** were less than **TFPHP** values, which proved that **BPHP** has higher inhibition efficiency and is more adsorbed than **TFPHP**.

UV spectral reflectance studies (Gloss value)

UV–visible diffuse reflectance spectroscopy of the CS surface was analyzed before and after immersion in 8M H_3PO_4 in the 200–700 nm range. The reflectance curves examined the function spectra of the coated film on the CS surface with different P_{ILs} inhibitor concentrations at different temperatures to identify iron phosphate. The blank sample (before corrosion) showed a low gloss value (*G* = 18.2, dull), as shown in Fig. 12. Conversely, all samples coated with P_{ILs} in different conditions were electrolytically corroded, where they showed higher gloss values [69]. In the case of the lower concentrations, the gloss value will be *G* = 21.7 (**BPHP**) and *G* = 19.2 (**TFPHP**), and optimum concentration *G* = 38.1 (**BPHP**) and *G* = 26 (**TFPHP**). Under different temperatures for **BPHP**, surface brightness was observed to increase by decreasing temperature to *G* = 38.1 at 293 K and *G* = 24.7 at 318 K. This indicates the reduction of the surface roughness and increasing the reflectance value as **BPHP** has more efficiency in inhibition rather than **TFPHP** due to forming a protective film on the metal surface.

XPS analysis

X-ray photoelectron spectroscopy (XPS) was utilized to analyze the elemental composition and chemical bonds which formed on the CS surface before and after the adsorption of P_{ILs}. This analytical technique played a crucial role in enhancing our comprehension of the underlying mechanism of adsorption.

XPS of iron, Fig. 13, showed two main peaks corresponding to $2p_{3/2}$ appeared at 711.48 (711.00) and $2p_{1/2}$ at 724.48(724.48) eV with a difference of 13 (13.48) eV, before and (after)adsorption indicating the presence of iron as various iron substrate Fe_3O_4 or FeO (Fe^{2+}) and Fe_2O_3 (Fe^{3+})[70,71]. However, The binding energy values in the

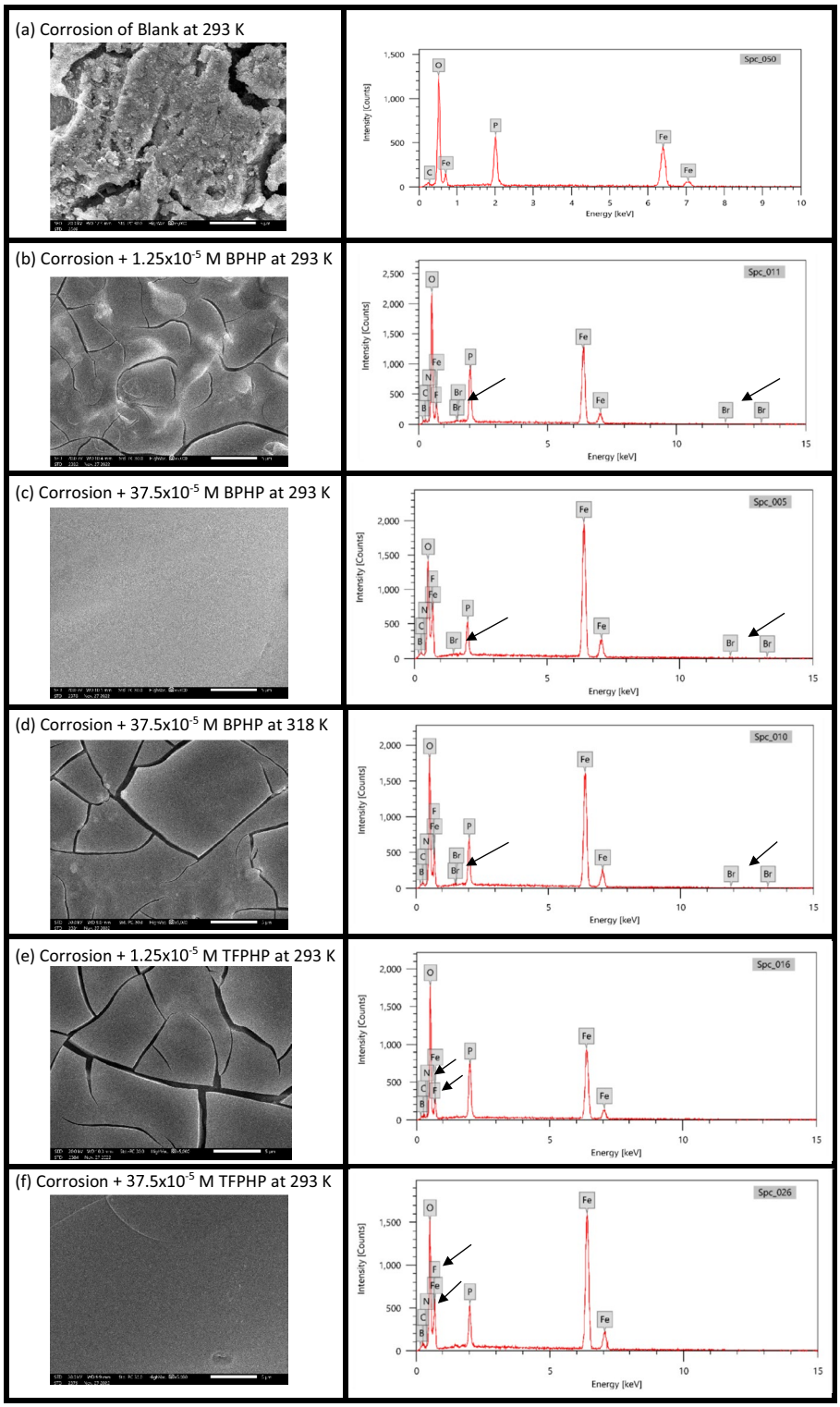

Figure 9. (**a**–**f**) SEM and EDX of CS surface with and without P_{ILs} at different temperatures and concentrations. (**a**) CS without P_{ILs}. (**b**, **e**) CS with 1.25×10^{-5} M P_{ILs} at 293 K (**c**, **f**) CS with 37.5×10^{-5} M P_{ILs} at 293 K (**d**) CS with 37.5×10^{-5} M **BPHP** at 318 K.

709–714 eV range confirm the presence of Fe (III) and/or Fe (II) and/or the formation of Fe–O–C bond[72]. Table 9 summarizes all peaks corresponding to Fe-binding energies before and after adsorption, showing that Different environments surround Fe-ions. The peaks at 712.59 and 727.43 eV with $\Delta E = 14.84$ eV may be attributed to the

No	Samples	Fe	C	O	P
a	Blank (293 K)	37.32	1.21	54.81	15.66
b	Corrosion + BPHP 1.25×10^{-5} M (293 K)	47.29	3.51	33.13	8.93
e	Corrosion + TFPHP 1.25×10^{-5} M (293 K)	39.44	3.37	36.97	10.26
c	Corrosion + BPHP 37.5×10^{-5} M (293 K)	62.66	3.34	21.55	5.29
f	Corrosion + TFPHP 37.5×10^{-5} M (293 K)	56.71	2.52	25.78	6.01
c	Corrosion + BPHP 37.5×10^{-5} M (293 K)	62.66	3.34	21.55	5.29
d	Corrosion + BPHP 37.5×10^{-5} M (318 K)	52.28	3.18	28.15	6.89

Table 7. Percentage of elemental analysis content derived from EDX spectra of P_{ILs}.

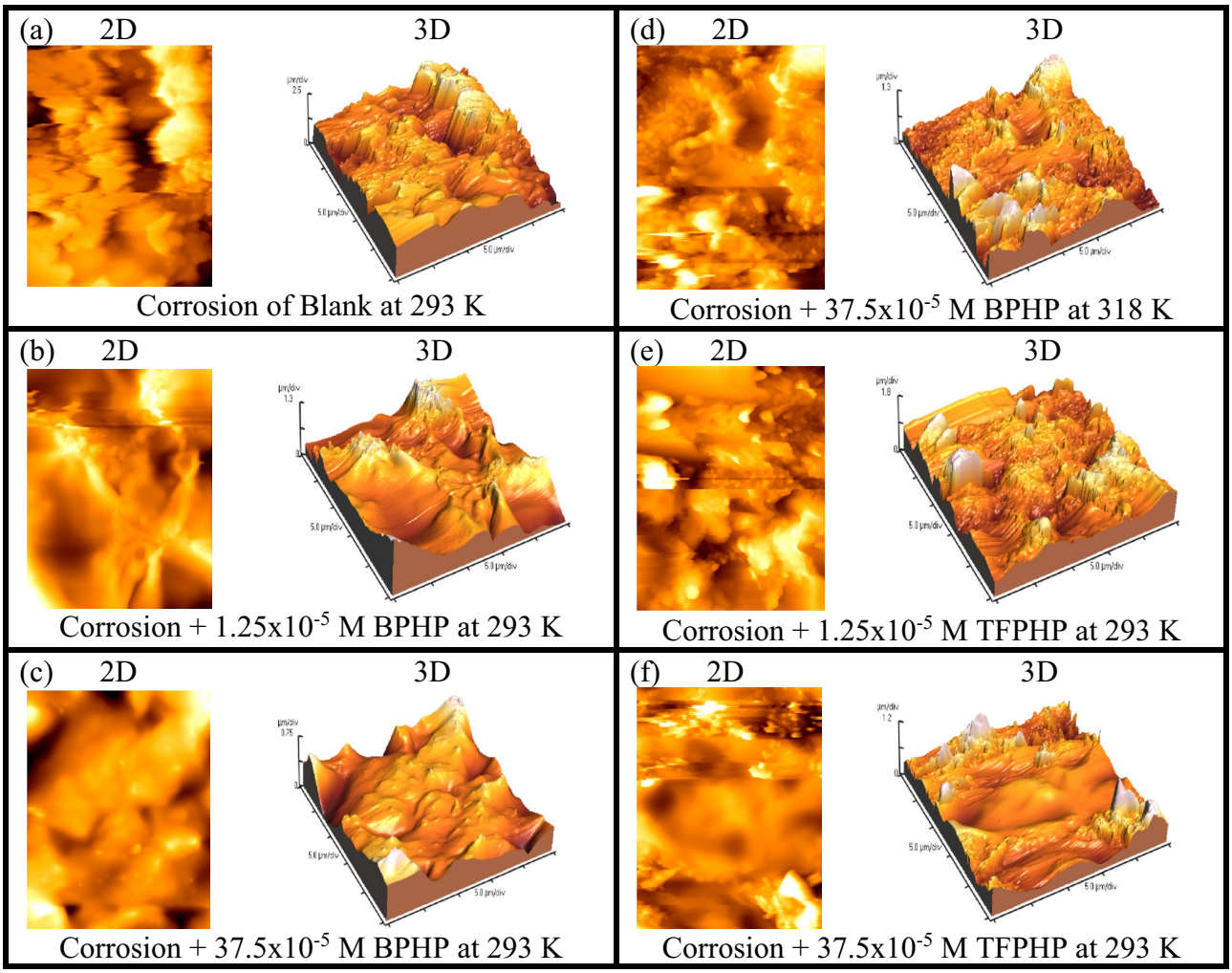

Figure 10. (**a**–**f**) AFM graphs of blank and P_{ILs} with different concentrations and temperatures. (**a**) CS without P_{ILs}. (**b**, **e**) CS with 1.25×10^{-5} M P_{ILs} at 293 K. (**c**, **f**) CS with 37.5×10^{-5} M P_{ILs} at 293 K (**d**) CS with 37.5×10^{-5} M **BPHP** at 318 K.

presence of Fe_3O_4. The appearance of a satellite of 719.32 eV and 715.89 eV ($\Delta E = 3.43$ eV) may correspond to bonding with fluoride ion[73].

Figure 14 shows the XPS spectra for C1s, O1s, P2p, and N1s, before and after adsorption. Three peaks of C1s at 284.99, 286.64, and 288.81 eV in the blank sample showed a slight shift in the B.E. values to 284.78, 286.53, and 288.38eV after treatment by inhibitor (Fig. 141-A, B). These peaks correspond to aromatic C, CN, and CO[72, 74]. A very large decrease in the peak area of peaks corresponding to CN or CO indicates the change in their media. For O1s spectrum was deconvoluted into two peaks at 531.64 and 533.18 eV corresponding to the Fe–O and O-C bonds, respectively, whereas the peaks were shifted to lower binding energies after adsorption at 531.58 and 529.97 eV, which could be attributed to its bonding to O-C, O-Fe(II)and/or Fe(III) ions (Fig. 142-A, B)[72]. P2p spectrum showed two deconvoluted peaks at 133.69 and 134.66 eV, which may attributed to PO_3

No	Samples	Ra (µm)	Rq (µm)	Rp-v (µm)	% I_{Eff}
a	Blank (293 K)	0.62	0.79	5.00	0.00
b	Corrosion + BPHP 1.25×10^{-5} M (293 K)	0.30	0.38	2.55	20.63
e	Corrosion + TFPHP 1.25×10^{-5} M (293 K)	0.44	0.56	3.68	15.87
c	Corrosion + BPHP 37.5×10^{-5} M (293 K)	0.16	0.20	1.50	76.19
f	Corrosion + TFPHP 37.5×10^{-5} M (293 K)	0.18	0.25	2.31	71.43
c	Corrosion + BPHP 37.5×10^{-5} M (293 K)	0.16	0.20	1.50	76.19
d	Corrosion + BPHP 37.5×10^{-5} M (318 K)	0.27	0.35	2.59	49.37

Table 8. Atomic force microscopic parameters for CS in 8 M H_3PO_4 with and without P_{ILs} at different concentrations and temperatures.

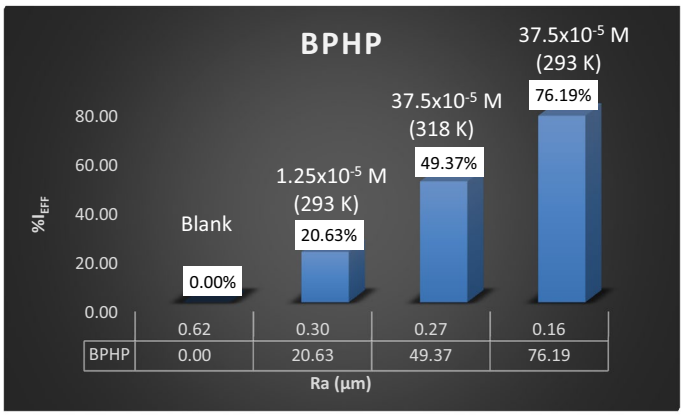

Figure 11. Relation between average roughness (*Ra*) and inhibition efficiency (%I_{Eff}) at different concentrations and temperatures for **BPHP** and blank.

P and PO_4P, respectively, showing a small shift after adsorption to 133.25 and 134.16, with a notable change in the peak area, Fig. 14(3-A, B)[75]. On the other hand, N1s showed a relative decrease in the peak intensity and peak areas that appeared at (400.15, 401.96) eV before adsorption and (399.08, 400.65) eV after adsorption. The binding energies could be attributed to N = C/N^+–C and N–H before that could have disappeared after adsorption (Fig. 14(4-A, B)[76].

The XPS scan after adsorption showed the presence of Boron (B), Fluorine (F), and Bromine (Br), which are shown in detail in Fig. 14(5–7). B1s displayed a characteristic boride peak at 189.1 eV, which is a smaller value than that of B-B that could be attributed to metal or carbon center attachment[77,78]. This is also can be evidenced by the difference in the N1s and C1s scans before and after adsorption. Fluorine showed F1s peak at 689.2 eV, which may be attributed to F–C bonding confirming its existence[79]. Bromine displayed two peaks corresponding to Br 3d with binding energies (B.E.) of 72.77 and 70.20 eV (ΔE = 2.57), which may be attributed to Br–C and/charge transfer from Br to iron in either oxidation state II and/or III. The presence of B, F and Be elements confirms the adsorption of **BPHP** as a protective inhibitor on the CS surface[80].

Computational investigation study

Quantum chemical descriptors, including E_{HOMO}, E_{LUMO}, Energy gap ($\Delta E = E_{LUMO} — E_{HOMO}$), chemical hardness, chemical softness, electronegativity, chemical potential, proton affinity, electrophilicity, and nucleophilicity, are well-known for being beneficial and efficient tools in investigations of metal corrosion. Sup.Tables (1–4) provide an overview of the selected P_{ILs} atoms of global molecular properties in the gas phase and aqueous solution[81,82]. The following will cover the relationships between descriptors and the order of corrosion inhibition efficiencies.

The Figured quantum compound properties for **BPHP** & **TFPHP** in the gas and fluid phases are given in Table 10. The geometry optimization is displayed in Fig. 15. The capacity of a particle to adsorb onto the metal surface is related to the hypothesis of frontier molecular orbital (*FMO*). E_{HOMO} alludes to the capacity of atoms to give electrons to the iron surface with empty "*d*" orbitals. The higher the energy level of the HOMO (E_{HOMO}), the more susceptible the ligand is to donate the electrons to the iron atoms to form a stronger bond. This could illustrate the compound's effectiveness in inhibiting the atoms' capacity to give electrons.

For this reason, **BPHP** is more effective than **TFPHP** in electron donation in the two phases. In concurrence with the calculation's outcomes, the E_{HOMO} of **BPHP** is the biggest. Subsequently, this compound is viewed as more reasonable for adsorption on the metallic surface through the pyridine ring, which is a rich source of electrons. In contrast, E_{LUMO} demonstrates the acceptance of electrons by the atoms where the lower value of E_{LUMO}, the more prominent the inhibitor effectiveness. The energy gap (ΔE_{gap}) plays a vital role in the reactivity of

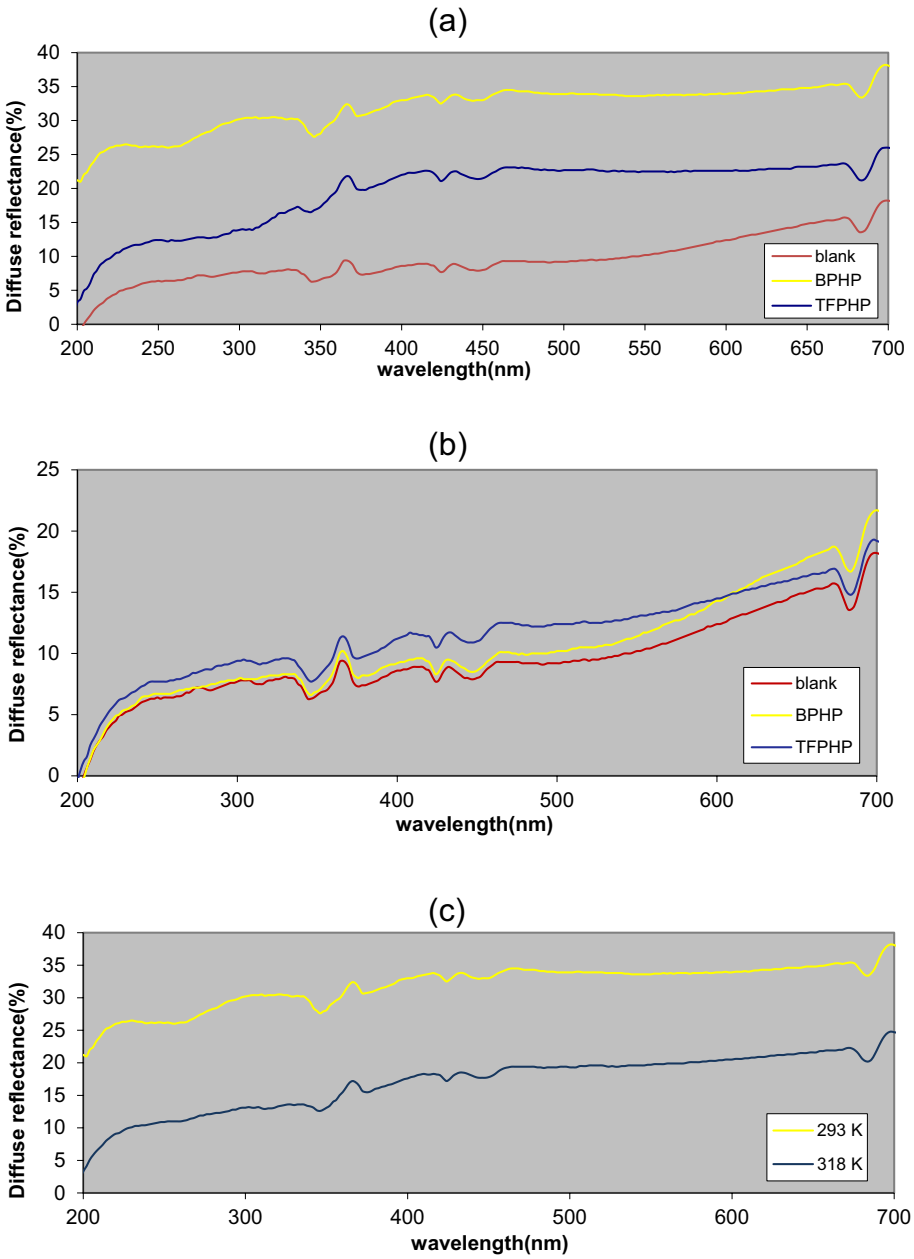

Figure 12. The gloss reflectance of P_{ILs}. (**a**) comparison between blank and P_{ILs} with 37.5×10^{-5} M P_{ILs} at 293 K. (**b**) comparison between blank and P_{ILs} at with 1.25×10^{-5} M P_{ILs} at 293 K. (**c**) comparison for **BPHP** with 37.5×10^{-5} M at different temperatures 293 and 318 K.

particles toward the metal surface. The lower value of ΔE_{gap} is the more tendency of atoms to adsorb on the metal surface. Table 10 shows that ΔE_{gap} for **TFPHP** in the gas phase is lower than in water. On the other hand, ΔE_{gap} values for **BPHP** are lower than those for **TFPHP**, showing that **BPHP** has a high reactivity in both phases. The calculations of (*FMOs*) of (**BPHP** & **TFPHP**) were performed by *B3LYP/6-311g (d,p)* Gaussian-09 program using density functional theory (DFT)[83,84], and the Gaussian View 5.0 was used to show the structural forms in Fig. 16.

The other parameters like hardness (η), softness (σ), electron back donation ($\Delta E_{b.d}$), work function (ΔN) and electronegativity (X) are calculated from the relations:

$$I = E_{HOMO} \quad A = E_{LUMO} \quad P_i = X \tag{14}$$

$$X = \frac{(I+A)}{2} \quad \eta = \frac{(I-A)}{2} \quad \sigma = \frac{1}{\eta} \quad \Delta E_{b.d} = \frac{-\eta}{4} \tag{15}$$

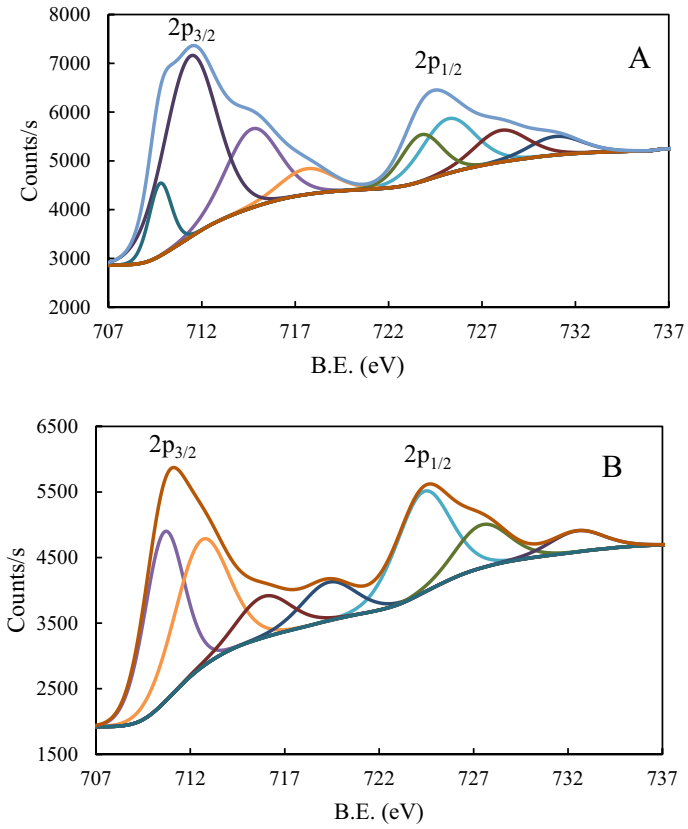

Figure 13. XPS scan of Iron (**A**) and after (**B**) adsorption.

Blanck			After adsorption		
$2p_{3/2}$	$2p_{1/2}$	ΔE	$2p_{3/2}$	$2p_{1/2}$	ΔE
709.77	723.74	13.97	710.60	724.34	13.74
711.38	725.18	13.80	712.59	727.43	14.84
717.61	730.94	13.33	719.32	732.48	13.16
714.70	728.02	13.32	715.89	-	-

Table 9. XPS binding energies and separation (ΔE) for iron before and after adsorption.

$$\omega = \frac{P_i^2}{2\eta} \quad \omega^- = \frac{(3I + A)^2}{16(I - A)} \quad \omega^+ = \frac{(I + 3A)^2}{16(I - A)} \quad \Delta\omega^{\pm} = \left(\omega^+ - \frac{1}{\omega^-}\right) \tag{16}$$

$$\Delta N = \frac{(X_{Fe} - -X)}{2(\eta_{Fe} + \eta)} \quad \Delta E_{steel/P_{ILs}} = \frac{(X_{Fe} - -X_{inh})^2}{4(\eta_{Fe} + \eta_{inh})} \tag{17}$$

where (I) ionization potential, (P_i) chemical potential, (A) electron affinity, (X_{Fe}) electronegativity of $Fe = 7$ eV, η_{Fe} The hardness of $Fe = 0$[85], ΔN is positive, meaning electrons transfer to the Fe surface from the inhibitors, and $\Delta E_{steel/inh}$ shows the interaction between **BPHP** or **TFPHP** and metal surface. The inhibitor **BPHP** has high work function, high softness, a less negative value of the back donation, high negative total energy ($T.E$), low hardness, high $\Delta E_{steel/PILs}$ and low electronegativity **BPHP** is more inhibition efficiency than **TFPHP** in the two phases.

The descriptors ω^+, ω^-, and $\Delta\omega^{\pm}$ mean electron accepting, electron-donating and net electrophilicity, respectively, where they increased as inhibition efficiency increased with decreasing energy gap[86]. On the other hand, dipole moment (μ_d) measures the polarity of the chemical bond in the molecules. In the aqueous phase, μ_d has a

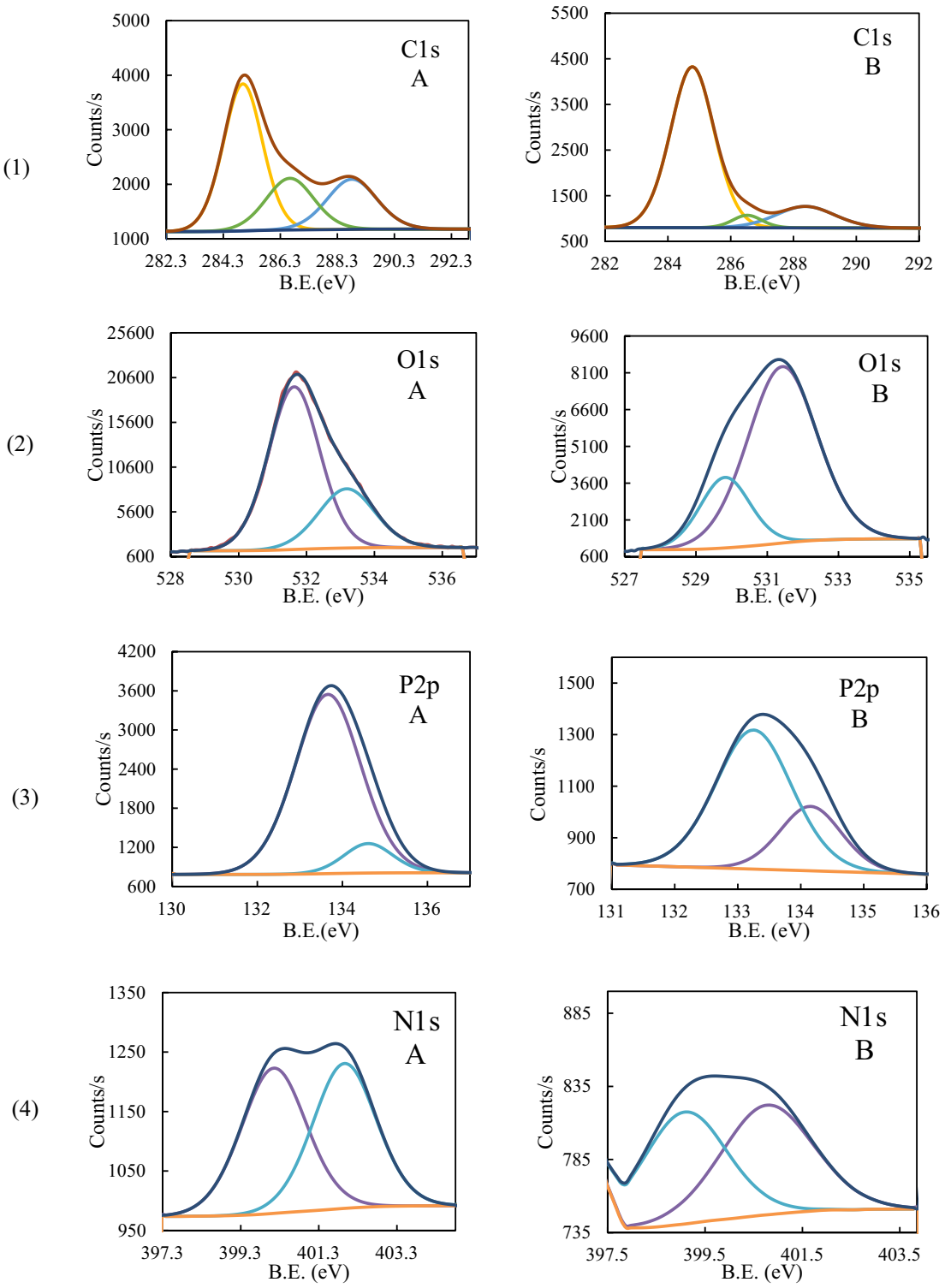

Figure 14. XPS scan of (1) C1s, (2) O1s, (3) P2p, and (4) N1s, before (**A**) and after (**B**) adsorption of **BPHP** and (5) B1s, (6) F1s, and (7) Br 3d after adsorption process.

larger value for **BPHP** than **TFPHP**, so **BPHP** is more anticorrosive, which matches experimental data. It is not a condition that all parameters agree with the practical information, but the majority agree with these results.

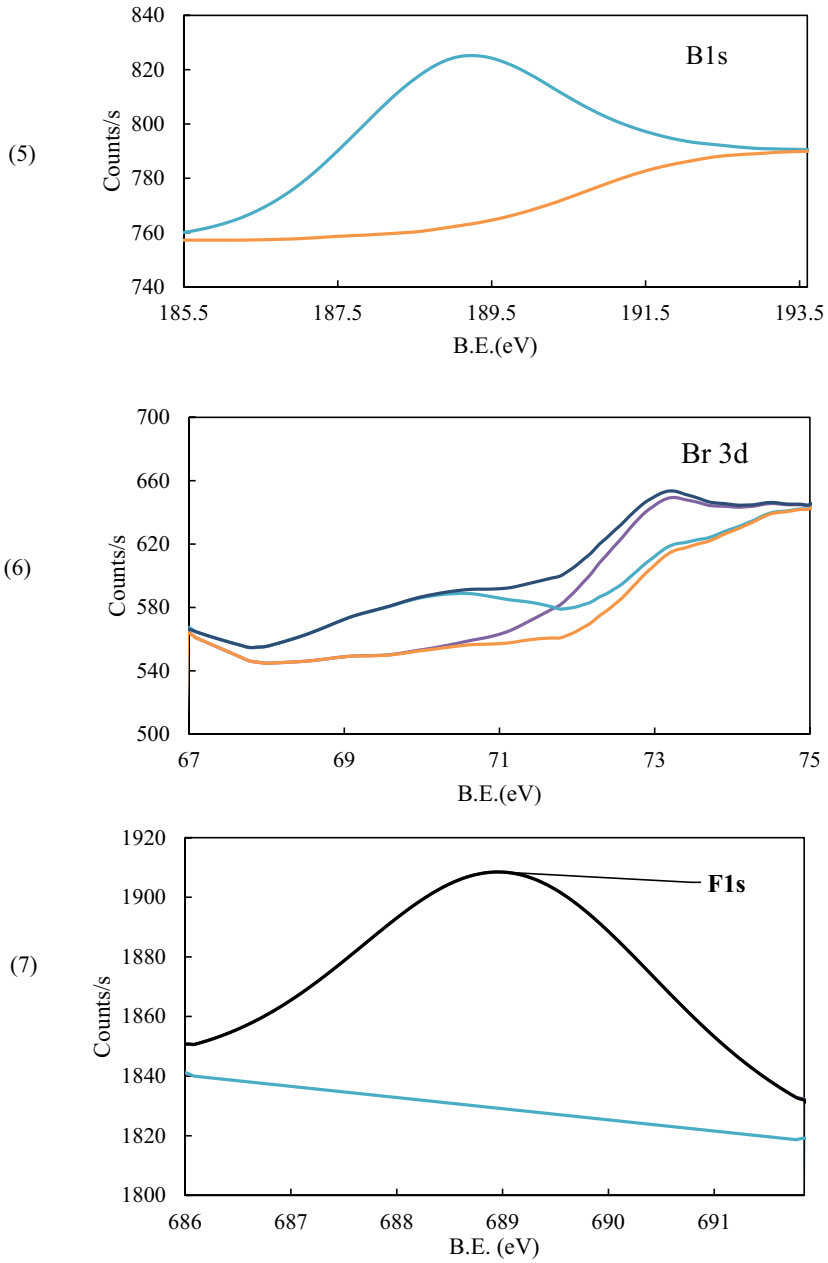

Figure 14. (continued)

Molecular electrostatic potential

The inhibitors' absorption on the metal surface is shown by the molecular electrostatic potential (MEP). In Fig. 16, the atoms of *O, N* and some of the *C* atoms for **BPHP** & **TFPHP** matrices carry negative charges. The highly negatively charged atoms can exchange electrons with the positive sites on the surface of the metal[87], Supplementary Tables 1–4 shows the distribution of the atomic charges of Mulliken on the atoms of **BPHP** & **TFPHP**. The best atoms in gas and aqueous phases are (*C5*, *O13*, *N25*, *O33*, *N34*, *C38*, *N48*, *O58*) for **BPHP** and (*C5*, *O12*, *N24*, *O32*, *N33*, *C37*, *N47*, *O57*) for **TFPHP**. So that atoms are responsible for a nucleophilic attack on the surface of the CS. Figure 16 shows the molecular electrostatic potential and electron density (*ED*) regions. The high *ED* is shown in red color, and the low *ED* is a blue color. *ED* decreases in the following order: red > orange > yellow > green > blue [84]. The high *ED* (yellow to red color) is localized on *O* and *N* atoms for **BPHP** & **TFPHP**. The low *ED* (green to blue color), on the other hand, is located on a few carbon atoms.

State	Gas		Aqueous	
P_{ILs}	BPHP	TFPHP	BPHP	TFPHP
E_{HOMO} (eV)	−7.3837	−7.9947	−7.2513	−7.5212
E_{LUMO} (eV)	−4.0686	−4.1582	−3.1932	−3.2128
ΔE_{gap} (eV)	3.3151	3.8365	4.0581	4.3084
I (eV)	7.3837	7.9947	7.2513	7.5212
A (eV)	4.0686	4.1582	3.1932	3.2128
X (eV)	5.7262	6.0765	5.2223	5.3670
P_i (eV)	−5.7262	−6.0765	−5.2223	−5.3670
μ_d (Debye)	11.8266	12.5062	17.5000	16.6904
η (eV)	1.6576	1.9183	2.0291	2.1542
σ (eV^{-1})	0.6033	0.5213	0.4928	0.4642
ω (eV)	9.8907	9.6242	6.7204	6.6857
$\Delta E_{b.d}$ (eV)	−0.4144	−0.4796	−0.5073	−0.5386
ΔN (eV)	0.3843	0.2407	0.4381	0.3790
T.E (Hartee)	−7522.6624	−3049.8514	−7522.6438	−3049.8387
$\Delta E_{steel/inh}$ (eV)	0.2447	0.1112	0.3894	0.3095
ω^- (eV)	12.9610	12.9022	9.5851	9.6385
ω^+ (eV)	7.2349	6.8258	4.3629	4.2715
$\Delta\omega^{\pm}$ (eV)	7.1577	6.7483	4.2585	4.1677

Table 10. Data of calculated quantum parameters for P_{ILs} in gas and aqueous phase.

Fukui indices and local dual descriptors

Fukui indices and Local Dual Descriptors describe the electrophilic and nucleophilic attack in the gas phase. The calculated condensed Fukui functions using Mulliken charges (f_k^+, f_k^-), local electrophilicity (ω_k^+, ω_k^-) and local softness (σ_k^+, σ_k^-) are reported in Sup.Tables (1,2). To facilitate the comparison between the possible sites for nucleophilic and electrophilic attacks on any atom k, we have calculated (Δf_k, $\Delta\sigma$ and $\Delta\omega$), which corresponds to the difference between (f_k^+, f_k^-), (σ_k^+, σ_k^-) and (ω_k^+, ω_k^-), respectively [10,88]. When comparing the atoms to determine the most reactive site consequently, the positive values of Δf, $\Delta\sigma$, $\Delta\omega$, i.e., >0, would be most favorable for a nucleophilic attack like (*N25*, *O33*, *N34*, *C38*, *C39*, *C45*, *N48*) atoms for **BPHP** & (*N24*, *O32*, *C37*, *C38*, *C44*, *N47*) atoms for **TFPHP**, on the other hand, if Δf, $\Delta\sigma$, $\Delta\omega > 0$, it would be favoured for an electrophilic attack like (*C5*, *O13*, *O58*) atoms for **BPHP** & (*O12* and *O57*) atoms for **TFPHP** and all are illustrated and described in the following equations and Fig. 17.

$$\begin{aligned} f_k^+ &= \rho_k(N+1)\rho_k(N)\ \left(\text{nucleophilic attack}\right) \\ f_k^- &= \rho_k(N)\rho_k(N-1)\ \left(\text{electrophilic attack}\right) \end{aligned} \tag{18}$$

$$\begin{aligned} \Delta f &= \left(f_k^+\right) - -\left(f_k^-\right) \\ \Delta\sigma &= \left(\sigma_k^+\right) - -\left(\sigma_k^-\right) \\ \Delta\omega &= \left(\omega_k^+\right) - -\left(\omega_k^-\right) \end{aligned} \tag{19}$$

where the electronic density site ρ with the number of electrons (N) at site k in a molecule.

Inhibition mechanism

According to the previous discussion, **BPHP** and **TFPHP** operate physically, chemically, or through both (physicochemical) adsorption to reduce the effectiveness of the employed solution (8 M H_3PO_4) on the CS surface. On the CS surface or due to the protonation of the inhibitor's heteroatoms in the bulk solution, charged species are present in the physical model. On the other hand, the chemisorption could be increased by transferring charge from the electron-rich centers (the lone pair of the heteroatom or the π-electrons of the unsaturated centers) of the inhibitor to the CS vacant d-orbitals (Fe^{2+})[89], which reduces surface erosion as shown in Fig. 18. By comparing the *N* (−0.3014) and *O* (−0.2952) of **TFPHP**, the calculated Milliken atomic charges of *N* (−0.3020) and *O* (−0.2968) of **BPHP** are more negative. Because the CF_3 polar group is more electron withdrawing than *Br*, the presence of the CF_3 may reduce the amount of charge transfer from the inhibitors to the CS surface. These findings might demonstrate how **BPHP** inhibits more effectively than **TFPHP**.

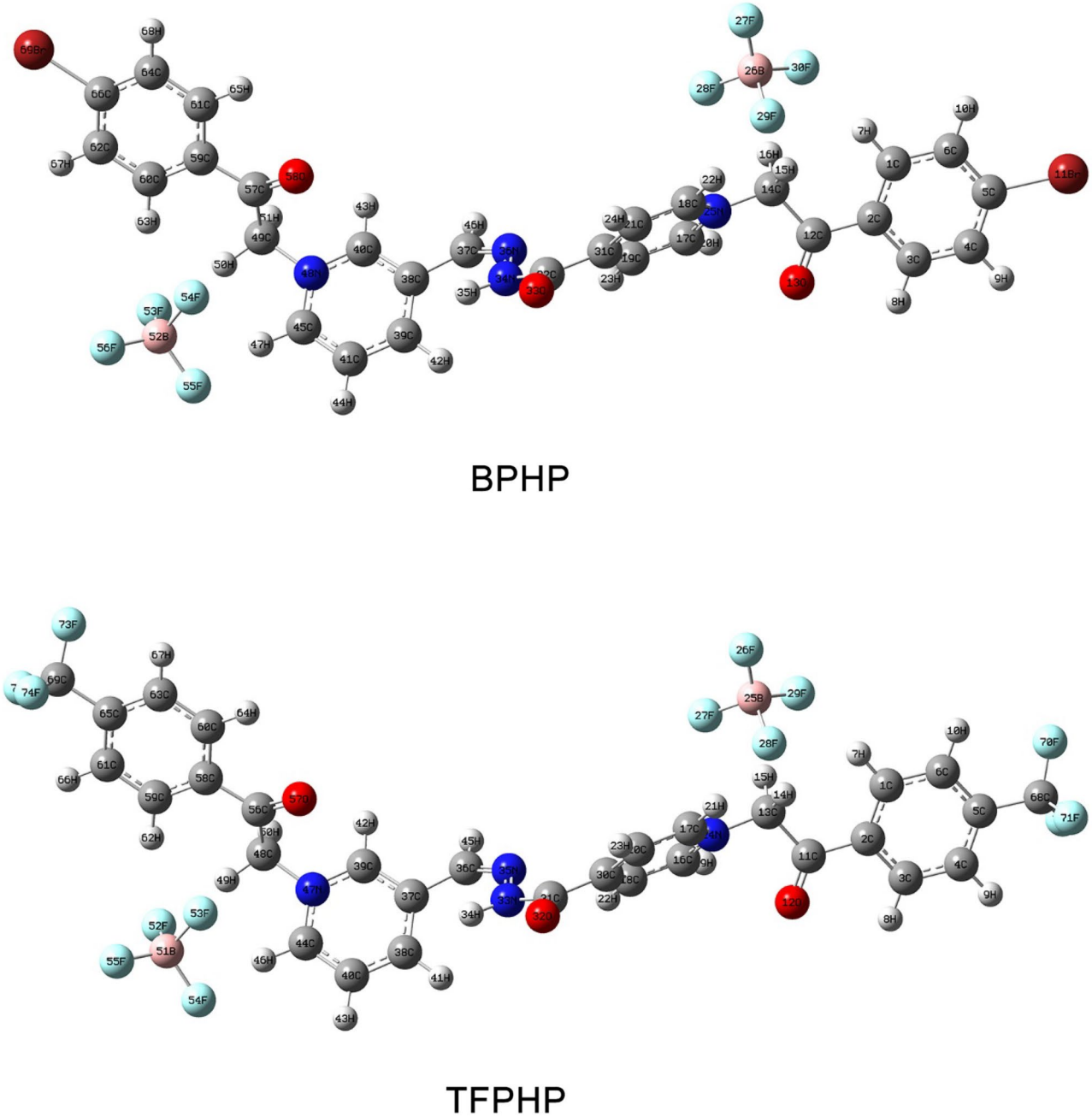

Figure 15. Optimized structures configuration geometry of P_{ILs}.

Conclusion

Finally, we found two new synthetic P_{ILs} with high efficiency of inhibition for C-steel surface and nontoxic where at different temperatures and concentrations, especially at 37.5×10^{-5} M with 293 K; **BPHP** and **TFPHP** were good inhibitors with inhibition percent 76.19% and 71.43% respectively. The electrochemical study of corrosion used to particular the anticorrosive new compounds where the best model of adsorption isotherm for them is the El-Awady model was applied. Temperature increase leads to decreased inhibition efficiency,

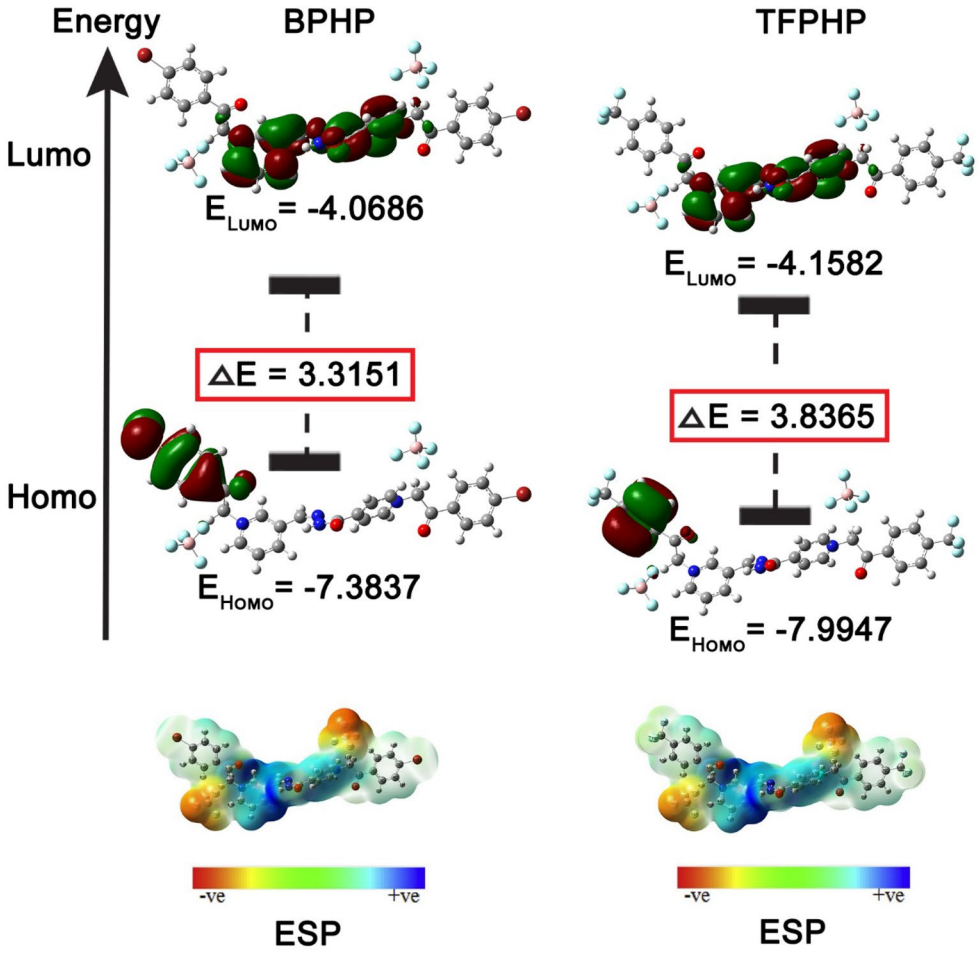

Figure 16. Frontier molecular orbital for HOMO–LUMO distribution energy and molecular electrostatic potential of P_{ILs}.

resulting in the effective activation energy value variation. Furthermore, surface studies like scanning electron microscopy-energy dispersive spectroscopy (SEM–EDS) revealed the protecting capability of the investigated inhibitors. An ultra-violet visible (UV–vis.) spectroscopy study confirms the formation of the Fe^{2+}–P_{ILs} complex. X-ray Photoelectron Spectroscopy (XPS) was conducted to study the formation of corrosion products and protective film over the mild steel surface. The theoretical study of DFT confirmed the experimental data and the mechanism, which showed the adsorption as physicochemical. The different characterizations showed that **BPHP** is better than **TFPHP** inhibitor due to the terminal group of **BPHP** being *Br* and CF_3 for **TFPHP**, where

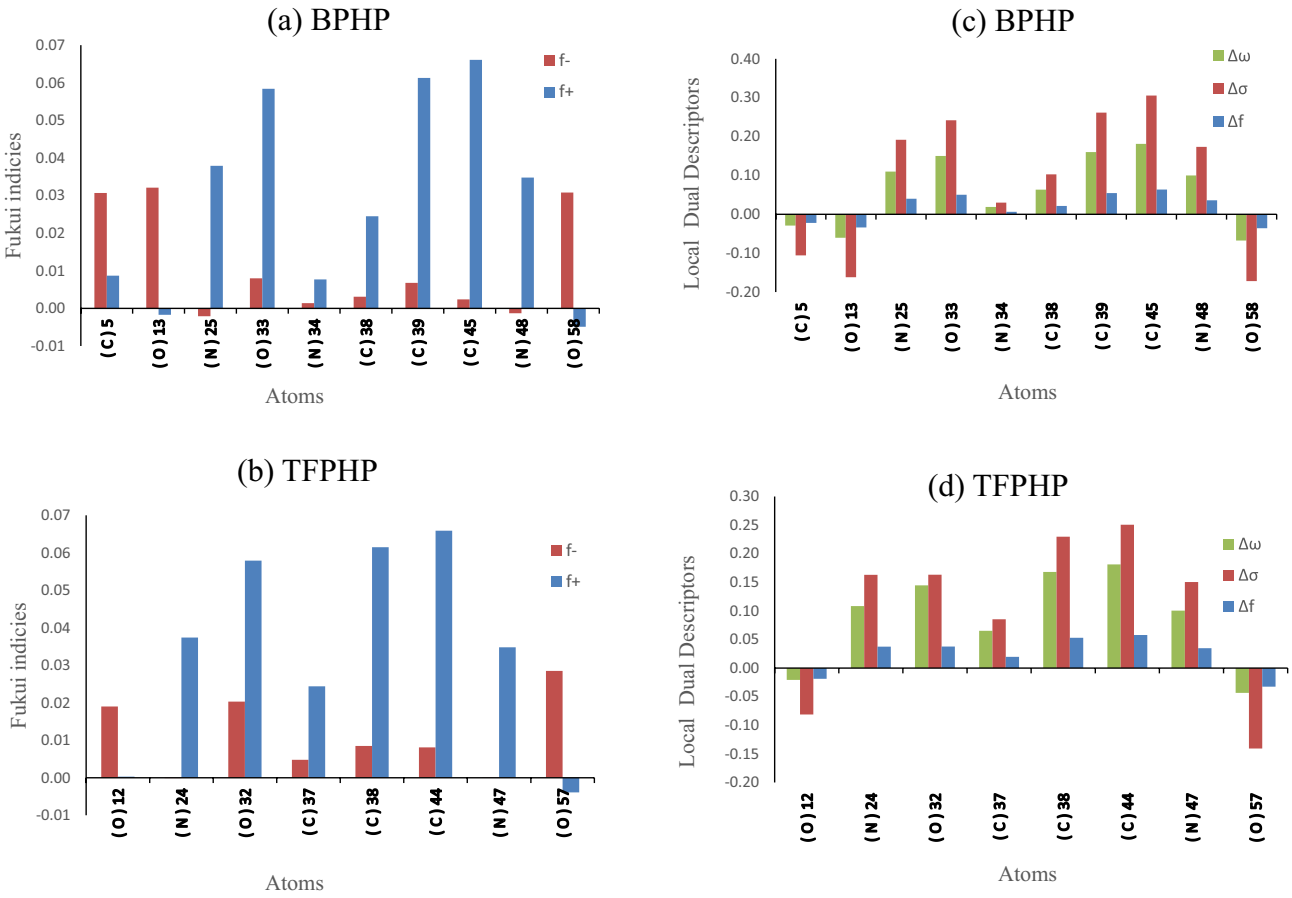

Figure 17. Fukui indices (**a**, **b**) and local dual descriptors (**c**, **d**) of different atoms with respect to Mulliken charges of P_{ILs}.

Br is more electron rich, softer, with positive Fukui parameters than CF_3. We hope to use the new P_{ILs} in another process, like Electroplating, to transfer layers of different metals to another metal surface.

Data availability

The data used and analyzed during the current study are available from the corresponding authors upon reasonable request.

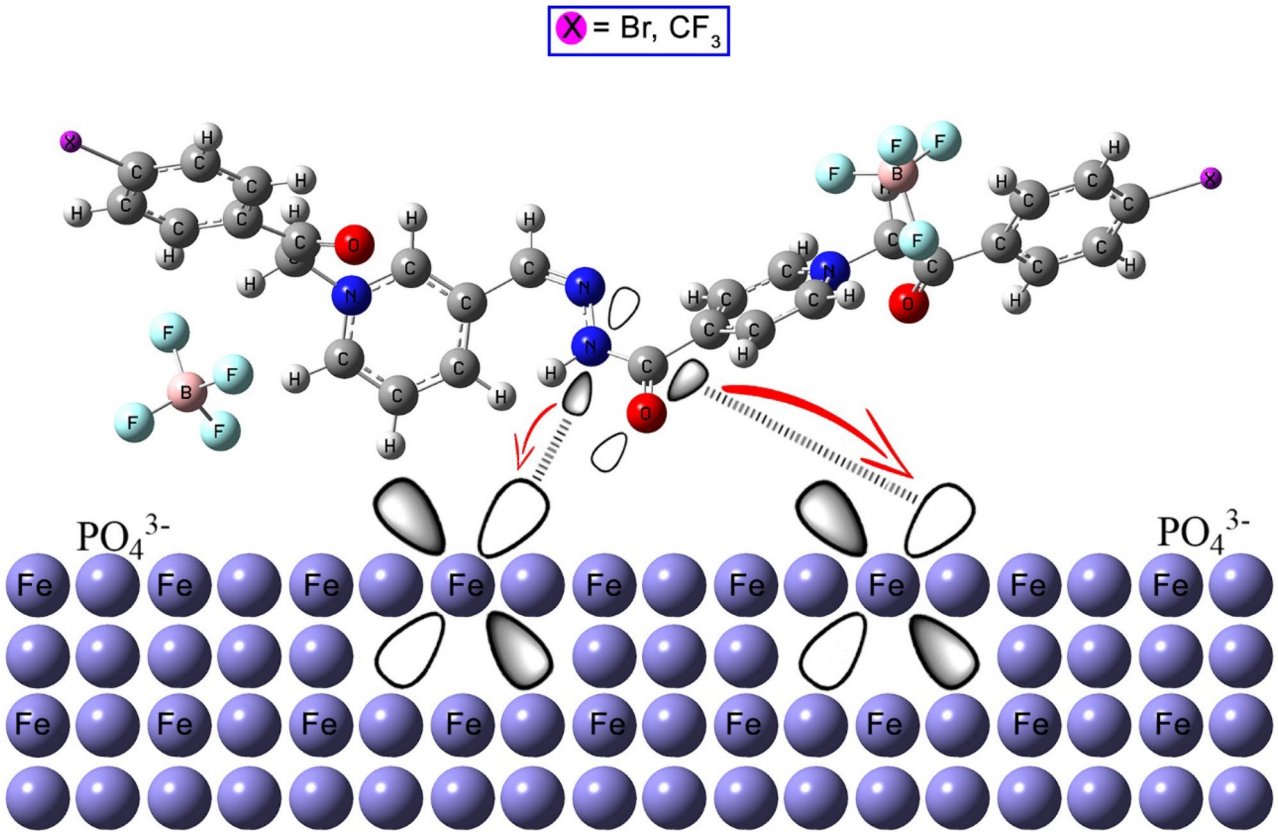

Figure 18. Schematic mechanism diagram of adsorption $P_{II_{LS}}$ on CS surface in 8M H_3PO_4.

Received: 10 July 2023; Accepted: 24 October 2023
Published online: 06 November 2023

References

1. Khamaysa, O. M. A. *et al.* Enhanced corrosion inhibition of carbon steel in HCl solution by a newly synthesized hydrazone derivative: Mechanism exploration from electrochemical, XPS, and computational studies. *J. Mol. Liq.* **315**, 113805 (2020).
2. Li, E., Li, Y., Liu, S. & Yao, P. Choline amino acid ionic liquids as green corrosion inhibitors of mild steel in acidic medium. *Colloids Surf. A* **657**, 130541 (2023).
3. Verma, C., Olasunkanmi, L. O., Ebenso, E. E., Quraishi, M. A. & Obot, I. B. Adsorption behavior of glucosamine-based, pyrimidine-fused heterocycles as green corrosion inhibitors for mild steel: experimental and theoretical studies. *J. Phys. Chem. C* **120**, 11598–11611 (2016).
4. Verma, C., Olasunkanmi, L., Obot, I., Ebenso, E. E. & Quraishi, M. 5-Arylpyrimido-[4, 5-b] quinoline-diones as new and sustainable corrosion inhibitors for mild steel in 1 M HCl: a combined experimental and theoretical approach. *RSC Adv.* **6**, 15639–15654 (2016).
5. Zakaria, K., Abbas, M. A. & Bedair, M. A. Herbal expired drug bearing glycosides and polysaccharides moieties as green and cost-effective oilfield corrosion inhibitor: Electrochemical and computational studies. *J. Mol. Liq.* **352**, 118689 (2022).
6. Verma, C., Olasunkanmi, L. O., Obot, I., Ebenso, E. E. & Quraishi, M. 2, 4-Diamino-5-(phenylthio)-5 H-chromeno [2, 3-b] pyridine-3-carbonitriles as green and effective corrosion inhibitors: gravimetric, electrochemical, surface morphology and theoretical studies. *RSC Adv.* **6**, 53933–53948 (2016).
7. Chen, Y. *et al.* Influence of H2S interaction with prestrain on the mechanical properties of high-strength X80 steel. *Int J Hydrog. Energy* **41**, 10412–10420 (2016).
8. Javidan, F., Heidarpour, A., Zhao, X.-L. & Minkkinen, J. Application of high strength and ultra-high strength steel tubes in long hybrid compressive members: Experimental and numerical investigation. *Thin-Walled Struct.* **102**, 273–285 (2016).
9. Desai, P. D., Pawar, C. B., Avhad, M. S. & More, A. P. Corrosion inhibitors for carbon steel: A review. *Vietnam J. Chem.* **61**, 15–42 (2023).
10. Moustafa, A. H. E., Abdel-Rahman, H. H., Mabrouk, D. F. & Omar, A. Z. Mass transfer role in electropolishing of carbone steel in H_3PO_4 containing amino acids: Electrochemical, computational, SEM/EDX, and stylus profilometer investigation. *Alex. Eng. J.* **61**, 6305–6327 (2022).
11. Moustafa, A. H. E., Abdel-Rahman, H. H., Awad, M. K., Naby, A. A. N. A. & Seleim, S. M. Molecular dynamic simulation studies and surface characterization of carbon steel corrosion with changing green inhibitors concentrations and temperatures. *Alex. Eng. J.* **61**, 2492–2519 (2022).
12. Abouzeid, F., Taha, A., Elsadek, M. & Othman, Y. The electro-polishing of C-steel in ortho-phosphoric acid containing methanolic plant extract. *Alex. Eng. J.* **61**, 4889–4909 (2022).
13. Taha, A. A. *et al.* Synthesis and evaluation of nonionic surfactants based on dimethylaminoethylamine: Electrochemical investigation and theoretical modeling as inhibitors during electropolishing in-ortho-phosphoric acid. *J. Mol. Liq.* **328**, 115421 (2021).
14. Li, E., Wang, Y., Zhang, Y., Zhao, S. & Yao, P. Deep desulfurization of model oil using green amino acid ionic liquids combined with H_2O_2. *Petrol. Sci. Technol.* **39**, 1116–1138 (2021).
15. Hajjaji, F. E. *et al.* New imidazolium ionic liquids as ecofriendly corrosion inhibitors for mild steel in hydrochloric acid (1 M): Experimental and theoretical approach. *J. Taiwan Inst. Chem. Eng.* **123**, 346–362 (2021).

16. Hernández-Bravo, R. *et al.* Experimental and theoretical study on the effectiveness of ionic liquids as corrosion inhibitors. *Comput. Theor. Chem.* **1210**, 113640 (2022).
17. Kobzar, Y. L. & Fatyeyeva, K. Ionic liquids as green and sustainable steel corrosion inhibitors: Recent developments. *Chem. Eng. J.* **425**, 131480 (2021).
18. Alrefaee, S. H. Effect of alkyl chain length and halide ions on the corrosion inhibition potential of imidazolium and pyridinium based ionic liquids: computational studies. *J. Mol. Liq.* **344**, 117848 (2021).
19. Cioc, R. C., Ruijter, E. & Orru, R. V. Multicomponent reactions: advanced tools for sustainable organic synthesis. *Green Chem.* **16**, 2958–2975 (2014).
20. Hart, W. E., Harper, J. B. & Aldous, L. The effect of changing the components of an ionic liquid upon the solubility of lignin. *Green Chem.* **17**, 214–218 (2015).
21. Dewilde, S., Dehaen, W. & Binnemans, K. Ionic liquids as solvents for PPTA oligomers. *Green Chem.* **18**, 1639–1652 (2016).
22. Mobin, M., Aslam, R., Salim, R. & Kaya, S. An investigation on the synthesis, characterization and anti-corrosion properties of choline based ionic liquids as novel and environmentally friendly inhibitors for mild steel corrosion in 5% HCl. *J. Colloid Interface Sci.* **620**, 293–312 (2022).
23. Hajipour, A. R. & Rafiee, F. Recent progress in ionic liquids and their applications in organic synthesis. *Organic Prepar. Proced. Int.* **47**, 249–308 (2015).
24. Hulsbosch, J., De Vos, D. E., Binnemans, K. & Ameloot, R. Biobased ionic liquids: solvents for a green processing industry?. *ACS Sustain. Chem. Eng.* **4**, 2917–2931 (2016).
25. Xing, D. Y., Dong, W. Y. & Chung, T.-S. Effects of different ionic liquids as green solvents on the formation and ultrafiltration performance of CA hollow fiber membranes. *Ind. Eng. Chem. Res.* **55**, 7505–7513 (2016).
26. Messali, M. *et al.* Synthesis, characterization, and POM analysis of novel bioactive imidazolium-based ionic liquids. *Med. Chem. Res.* **24**, 1387–1395 (2015).
27. Rezki, N. *et al.* An eco-friendly ultrasound-assisted synthesis of novel fluorinated pyridinium salts-based hydrazones and antimicrobial and antitumor screening. *Int. J. Mol. Sci.* **17**, 766 (2016).
28. Rezki, N. *et al.* Green ultrasound versus conventional synthesis and characterization of specific task pyridinium ionic liquid hydrazones tethering fluorinated counter anions: Novel inhibitors of fungal Ergosterol biosynthesis. *Molecules* **22**, 1532 (2017).
29. Albalawi, A. H. *et al.* Microwave-assisted synthesis of some potential bioactive imidazolium-based room-temperature ionic liquids. *Molecules* **23**, 1727 (2018).
30. Aljuhani, A. *et al.* Novel pyridinium based ionic liquids with amide tethers: Microwave assisted synthesis, molecular docking and anticancer studies. *J. Mol. Liq.* **285**, 790–802 (2019).
31. Rezki, N. *et al.* Synthesis, characterization, DNA binding, anticancer, and molecular docking studies of novel imidazolium-based ionic liquids with fluorinated phenylacetamide tethers. *ACS Omega* **5**, 4807–4815 (2020).
32. Al-Sodies, S. A. *et al.* Microwave and conventional synthesis of ester based dicationic pyridinium ionic liquids carrying hydrazone linkage: DNA binding, anticancer and docking studies. *J. Mol. Struct.* **1207**, 127756 (2020).
33. Brunner, M., Li, H., Zhang, Z., Zhang, D. & Atkin, R. Pinewood pyrolysis occurs at lower temperatures following treatment with choline-amino acid ionic liquids. *Fuel* **236**, 306–312 (2019).
34. Verma, C., Ebenso, E. E. & Quraishi, M. Ionic liquids as green and sustainable corrosion inhibitors for metals and alloys: An overview. *J. Mol. Liq.* **233**, 403–414 (2017).
35. Fedorov, M. V. & Kornyshev, A. A. Ionic liquids at electrified interfaces. *Chem. Rev.* **114**, 2978–3036 (2014).
36. Egorova, K. S., Gordeev, E. G. & Ananikov, V. P. Biological activity of ionic liquids and their application in pharmaceutics and medicine. *Chem. Rev.* **117**, 7132–7189 (2017).
37. Sun, X., Luo, H. & Dai, S. Ionic liquids-based extraction: a promising strategy for the advanced nuclear fuel cycle. *Chem. Rev.* **112**, 2100–2128 (2012).
38. Zhang, Q. & Shreeve, J. N. M. Energetic ionic liquids as explosives and propellant fuels: a new journey of ionic liquid chemistry. *Chem. Rev.* **114**, 10527–10574 (2014).
39. Goossens, K., Lava, K., Bielawski, C. W. & Binnemans, K. Ionic liquid crystals: Versatile materials. *Chemical reviews* **116**, 4643–4807 (2016).
40. Kumar, V. & Malhotra, S. V. in *Ionic liquid applications: Pharmaceuticals, therapeutics, and biotechnology* 1–12 (ACS Publications, 2010).
41. Abdel-Basset, T. A. *et al.* Dielectric response and density functional theory assessment of fluorinated dicationic pyridinium ionic liquids. *Nano Select* **3**, 1574–1582 (2022).
42. Selva Kumar, R. & Chandrasekaran, V. Valoniopsis pachynema extract as a green inhibitor for corrosion of brass in 0.1 N phosphoric acid solution. *Metallurgical and Materials Transactions B* **47**, 891–898 (2016).
43. Beniken, M. *et al.* Adsorption behavior and corrosion inhibition mechanism of a polyacrylamide on C–steel in 0.5 M H2SO4: Electrochemical assessments and molecular dynamic simulation. *J. Mol. Liq.* **348**, 118022. https://doi.org/10.1016/j.molliq.2021.118022 (2022).
44. Kokalj, A. On the use of the Langmuir and other adsorption isotherms in corrosion inhibition. *Corros. Sci.* **217**, 111112. https://doi.org/10.1016/j.corsci.2023.111112 (2023).
45. Ebenso, E. E. & Obot, I. B. Inhibitive properties, thermodynamic characterization and quantum chemical studies of secnidazole on mild steel corrosion in acidic medium. *Int. J. Electrochem. Sci.* **5**, 2012–2035. https://doi.org/10.1016/s1452-3981(23)15402-2 (2010).
46. Abdul Rahiman, A. F. S. & Sethumanickam, S. Corrosion inhibition, adsorption and thermodynamic properties of poly(vinyl alcohol-cysteine) in molar HCl. *Arab. J. Chem.* **10**, S3358–S3366, https://doi.org/10.1016/j.arabjc.2014.01.016 (2017).
47. El Hamdani, N., Fdil, R., Tourabi, M., Jama, C. & Bentiss, F. Alkaloids extract of *Retama monosperma* (L.) Boiss. seeds used as novel eco-friendly inhibitor for carbon steel corrosion in 1 M HCl solution: Electrochemical and surface studies. *Appl. Surf. Sci.* **357**, 1294–1305 (2015).
48. Obi-Egbedi, N. O., Obot, I. B. & Umoren, S. A. *Spondias mombin* L. as a green corrosion inhibitor for aluminium in sulphuric acid: Correlation between inhibitive effect and electronic properties of extracts major constituents using density functional theory. *Arab. J. Chem.* **5**, 361–373, https://doi.org/10.1016/j.arabjc.2010.09.002 (2012).
49. Gadow, H. S., Farghaly, T. A. & Eldesoky, A. M. In an acidic environment, perimidin-10-one derivatives were evaluated as potential copper corrosion inhibitors (experimental and theoretical examinations). *J. Bio- and Tribo-Corros.* **8**, https://doi.org/10.1007/s40735-022-00650-8 (2022).
50. Singh, A. K. & Quraishi, M. A. Effect of cefazolin on the corrosion of mild steel in HCl solution. *Corros. Sci.* **52**, 152–160. https://doi.org/10.1016/j.corsci.2009.08.050 (2010).
51. Parthipan, P., Cheng, L. & Rajasekar, A. Glycyrrhiza glabra extract as an eco-friendly inhibitor for microbiologically influenced corrosion of API 5LX carbon steel in oil well produced water environments. *J. Mol. Liq.* **333**, 115952 (2021).
52. Naghi Tehrani, M. E. H., Ghahremani, P., Ramezanzadeh, M., Bahlakeh, G. & Ramezanzadeh, B. Theoretical and experimental assessment of a green corrosion inhibitor extracted from Malva sylvestris. *J. Environ. Chem. Eng.* **9**, 105256. https://doi.org/10.1016/j.jece.2021.105256 (2021).
53. Huang, L. *et al.* Corrosion resistance and antibacterial activity of procyanidin B2 as a novel environment-friendly inhibitor for Q235 steel in 1 M HCl solution. *Bioelectrochemistry* **143**, 107969. https://doi.org/10.1016/j.bioelechem.2021.107969 (2022).

54. Obot, I. B. & Obi-Egbedi, N. O. Anti-corrosive properties of xanthone on mild steel corrosion in sulphuric acid: Experimental and theoretical investigations. *Curr. Appl. Phys.* **11**, 382–392. https://doi.org/10.1016/j.cap.2010.08.007 (2011).
55. Alamry, K. A., Khan, A., Aslam, J., Hussein, M. A. & Aslam, R. Corrosion inhibition of mild steel in hydrochloric acid solution by the expired Ampicillin drug. *Sci Rep* **13**, 6724. https://doi.org/10.1038/s41598-023-33519-y (2023).
56. Obi-Egbedi, N. O. & Obot, I. B. Inhibitive properties, thermodynamic and quantum chemical studies of alloxazine on mild steel corrosion in H2SO4. *Corros. Sci.* **53**, 263–275. https://doi.org/10.1016/j.corsci.2010.09.020 (2011).
57. Beda, R. H. B., Niamien, P. M., Avo Bilé, E. B. & Trokourey, A. Inhibition of Aluminium Corrosion in 1.0 M HCl by Caffeine: Experimental and DFT Studies. *Adv. Chem.* **2017**, 1–10, https://doi.org/10.1155/2017/6975248 (2017).
58. Aslam, R. *et al.* Proline nitrate ionic liquid as high temperature acid corrosion inhibitor for mild steel: Experimental and molecular-level insights. *J. Ind. Eng. Chem.* **100**, 333–350. https://doi.org/10.1016/j.jiec.2021.05.005 (2021).
59. Zarrouk, A., Hammouti, B., Zarrok, H., Al-Deyab, S. & Messali, M. TInt. J. . emperature effect, activation energies and thermodynamic adsorption studies of L-cysteine methyl ester hydrochloride as copper corrosion inhibitor in nitric acid 2M. . *Electrochem.* (Sci 6, 6261–6274 (2011).).
60. Alamry, K. A., Aslam, R., Khan, A., Hussein, M. A. & Tashkandi, N. Y. Evaluation of corrosion inhibition performance of thiazolidine-2,4-diones and its amino derivative: Gravimetric, electrochemical, spectroscopic, and surface morphological studies. *Process Saf. Environ. Prot.* **159**, 178–197. https://doi.org/10.1016/j.psep.2021.12.061 (2022).
61. Hmamou, D. B. *et al.* Experimental and theoretical studies of the adsorption and corrosion inhibition of 6-phenylpyridazine-3(2H)-thione on Carbon Steel in 2.0 M H3PO4 solution. *Int. J. Electrochem. Sci.* **9**, 120–138, https://doi.org/10.1016/s1452-3981(23)07702-7 (2014).
62. Hameed, R. A. *et al.* Expired dulcolax drug as corrosion inhibitor for low carbon steel in acidic environment. *Int. J. Electrochem. Sci.* **17**, 220655 (2022).
63. Elaryian, H. M., Bedair, M. A., Bedair, A. H., Aboushahba, R. M. & Fouda, A. E. S. Corrosion mitigation for steel in acid environment using novel p-phenylenediamine and benzidine coumarin derivatives: synthesis, electrochemical, computational and SRB biological resistivity. *RSC Adv* **12**, 29350–29374. https://doi.org/10.1039/d2ra05803k (2022).
64. Mehta, H., Kaur, G., Chaudhary, G. R. & Prabhakar, N. Assessment of bio-corrosion inhibition ability of Hafnium based cationic metallosurfactant on iron surface. *Corros. Sci.* **179**, 109101 (2021).
65. Hafez, B., Mokhtari, M., Elmsellem, H. & Steli, H. Environmentally friendly inhibitor of the corrosion of mild steel: Commercial oil of Eucalyptus. *Int. J. Corros. Scale Inhibition* **8**, 573–585 (2019).
66. Chkirate, K. *et al.* Corrosion inhibition potential of 2-[(5-methylpyrazol-3-yl)methyl]benzimidazole against carbon steel corrosion in 1 M HCl solution: Combining experimental and theoretical studies. *J. Mol. Liq.* **321**, 114750. https://doi.org/10.1016/j.molliq.2020.114750 (2021).
67. Kaya, F., Solmaz, R. & Geçibesler, İH. Adsorption and corrosion inhibition capability of Rheum ribes root extract (Işgın) for mild steel protection in acidic medium: A comprehensive electrochemical, surface characterization, synergistic inhibition effect, and stability study. *J. Mol. Liq.* **372**, 121219. https://doi.org/10.1016/j.molliq.2023.121219 (2023).
68. Shenoy K, V., Venugopal, P. P., Reena Kumari, P. D. & Chakraborty, D. Anti-corrosion investigation of a new nitro veratraldehyde substituted imidazopyridine derivative Schiff base on mild steel surface in hydrochloric acid medium: Experimental, computational, surface morphological analysis. *Mater. Chem. Phys.* **281**, 125855, https://doi.org/10.1016/j.matchemphys.2022.125855 (2022).
69. Kumar, H., Karthikeyan, S., Vivekanand, P. & Kamaraj, P. The inhibitive effect of cloxacillin on mild steel corrosion in 2 N Sulphuric acid medium. *Mater. Today: Proc.* **36**, 898–902 (2021).
70. Chastain, J. & King, R. C. Jr. Handbook of X-ray photoelectron spectroscopy. *Perkin-Elmer Corp* **40**, 221 (1992).
71. Tan, B. J., Klabunde, K. J. & Sherwood, P. M. X-ray photoelectron spectroscopy studies of solvated metal atom dispersed catalysts. Monometallic iron and bimetallic iron-cobalt particles on alumina. *Chem. Mater.* **2**, 186–191 (1990).
72. Khalil, T. E., Elbadawy, H. A. & El-Dissouky, A. Synthesis, characterization and physicochemical studies of new chelating resin 1, 8-(3, 6-dithiaoctyl)-4-polyvinylbenzenesulphonate (dpvbs) and its metallopolymer Cu(II), Ni(II), Co(II) and Fe(III) complexes. *J. Mol. Struct.* **1154**, 100–113. https://doi.org/10.1016/j.molstruc.2017.10.033 (2018).
73. Kasrai, M. & Urch, D. S. Electronic structure of iron(II) and (III) fluorides using X-ray emission and X-ray photoelectron spectroscopies. *J. Chem. Soc. Faraday Trans. 2: Mol. Chem. Phys.* **75**, 1522–1531, https://doi.org/10.1039/F29797501522 (1979).
74. Ding-Bo, W., Bao-Hua, C., Bing, Z. & Yong-Xiang, M. XPS study of aroylhydrazones containing triazole and their chelates. *Polyhedron* **16**, 2625–2629. https://doi.org/10.1016/S0277-5387(96)00606-7 (1997).
75. Peng, Y., Zhai, P., Shi, Y., Jiang, H. & Li, G. Band alignment and photocatalytic activity of monoclinic $BiVO_4$ (0 1 0) and (1 0 0) films with $SrTiO_3$. *Appl. Surf. Sci.* **618**, 156482 (2023).
76. Ayiania, M. *et al.* Deconvoluting the XPS spectra for nitrogen-doped chars: An analysis from first principles. *Carbon* **162**, 528–544. https://doi.org/10.1016/j.carbon.2020.02.065 (2020).
77. Moulder, J. F., Stickle, W. F., Sobol, P. E. & Bomben, K. D. Handbook of X-ray photoelectron spectroscopy: a reference book of standard spectra for identification and interpretation of XPS data, 1992. *Google Scholar There is no corresponding record for this reference* (2000).
78. Greczynski, G. & Hultman, L. Towards reliable X-ray photoelectron spectroscopy: Sputter-damage effects in transition metal borides, carbides, nitrides, and oxides. *Appl. Surf. Sci.* **542**, 148599. https://doi.org/10.1016/j.apsusc.2020.148599 (2021).
79. Lee, J.-M. *et al.* A high resolution XPS study of sidewall functionalized MWCNTs by fluorination. *J. Ind. Eng. Chem.* **15**, 66–71. https://doi.org/10.1016/j.jiec.2008.08.010 (2009).
80. Wang, L. *et al.* Adsorption mechanism of quaternary ammonium corrosion inhibitor on carbon steel surface using ToF-SIMS and XPS. *Corros. Sci.* **213**, 110952 (2023).
81. Abdallah, M. *et al.* Insight of corrosion mitigation performance of SABIC iron in 0.5 M HCl solution by tryptophan and histidine: Experimental and computational approaches. *Int. J. Hydrog. Energy* **47**, 12782–12797, https://doi.org/10.1016/j.ijhydene.2022.02.007 (2022).
82. Guo, L. *et al.* Anticorrosive effects of some thiophene derivatives against the corrosion of iron: A computational study. *Front Chem* **6**, 155. https://doi.org/10.3389/fchem.2018.00155 (2018).
83. Wang, Y., Chen, Z. & Hu, L. . Determining the geometric surface area of mesoporous materials. *J. Phys. Chem. C* **C 127**, 4799–4807 (2023).
84. Hsissou, R. Review on epoxy polymers and its composites as a potential anticorrosive coatings for carbon steel in 3.5% NaCl solution: Computational approaches. *J. Mol. Liq.* **336**, 116307, https://doi.org/10.1016/j.molliq.2021.116307 (2021).
85. El-Azabawy, O. E. *et al.* Studying the temperature influence on carbon steel in sour petroleum media using facilely-designed Schiff base polymers as corrosion inhibitors. *J. Mol. Struct.* **1275**, 134518. https://doi.org/10.1016/j.molstruc.2022.134518 (2023).
86. Allal, H., Belhocine, Y. & Zouaoui, E. Computational study of some thiophene derivatives as aluminium corrosion inhibitors. *J. Mol. Liq.* **265**, 668–678. https://doi.org/10.1016/j.molliq.2018.05.099 (2018).
87. Abdelshafi, N. S., Sadik, M. A., Shoeib, M. A. & Halim, S. A. Corrosion inhibition of aluminum in 1 M HCl by novel pyrimidine derivatives, EFM measurements, DFT calculations and MD simulation. *Arab. J. Chem.* **15**, 103459. https://doi.org/10.1016/j.arabjc.2021.103459 (2022).
88. Sundaram, R. G., Vengatesh, G. & Sundaravadivelu, M. Surface morphological and quantum chemical studies of some expired drug molecules as potential corrosion inhibitors for mild steel in chloride medium. *Surf. Interfaces* **22**, 100841. https://doi.org/10.1016/j.surfin.2020.100841 (2021).

89. Mobin, M., Aslam, R., Salim, R. & Kaya, S. An investigation on the synthesis, characterization and anti-corrosion properties of choline based ionic liquids as novel and environmentally friendly inhibitors for mild steel corrosion in 5% HCl. *J Colloid Interface Sci* **620**, 293–312. https://doi.org/10.1016/j.jcis.2022.04.036 (2022).

Author contributions

A.H.E.M., H.H.A-R., and M.H. finished the study design. M.R.A. and N.R. prepare and characterize the organic compounds. A.H.E.M. and S.A.A.B. completed experimental studies. A.H.E.M., M.H. and S.A.A.B. finished the data analysis. H.H.A-R., M.H. and S.A.A.B. finished the manuscript editing. All authors read and approved the final manuscript.

Funding

Open access funding provided by The Science, Technology & Innovation Funding Authority (STDF) in cooperation with The Egyptian Knowledge Bank (EKB).

Competing interests

The authors declare no competing interests.

Additional information

Supplementary Information The online version contains supplementary material available at https://doi.org/10.1038/s41598-023-45822-9.

Correspondence and requests for materials should be addressed to A.H.E.M.

Reprints and permissions information is available at www.nature.com/reprints.

Publisher's note Springer Nature remains neutral with regard to jurisdictional claims in published maps and institutional affiliations.

Open Access This article is licensed under a Creative Commons Attribution 4.0 International License, which permits use, sharing, adaptation, distribution and reproduction in any medium or format, as long as you give appropriate credit to the original author(s) and the source, provide a link to the Creative Commons licence, and indicate if changes were made. The images or other third party material in this article are included in the article's Creative Commons licence, unless indicated otherwise in a credit line to the material. If material is not included in the article's Creative Commons licence and your intended use is not permitted by statutory regulation or exceeds the permitted use, you will need to obtain permission directly from the copyright holder. To view a copy of this licence, visit http://creativecommons.org/licenses/by/4.0/.

© The Author(s) 2023